UNIVERSITÀ DEGLI STUDI DI CAGLIARI

DOTTORATO DI RICERCA
Fisica Nucleare, Subnucleare e Astrofisica
Ciclo XXV

Monte Carlo simulation studies for spatially fractionated radiation therapy techniques

Settore scientifico disciplinare di afferenza
FIS/07 Fisica Applicata

Presentata da:	Giovanna Rosa Fois
Coordinatore Dottorato:	Prof. P. Ruggerone
Relatori:	Prof. P. Randaccio
	Dr. Y. Prezado

Esame finale anno accademico 2011-2012

A bois ki m'azes pesau...

"Le beaucoup savoir apporte l'occasion de plus douter"
Montaigne

ACKNOWLEDGEMENTS

My first debt of gratitude must go to Dr. Yolanda Prezado. She patiently provided encouragement and useful advices along the years of the doctoral program.

Special thanks to Dr. Avraham Dilmanian for his support, guidance and helpful suggestions during my training period at Brookhaven National Lab.

Finally, I want to thank Prof. Paolo Randaccio for giving me great freedom to pursue independent work.

Contents

Introduction

Cancer is a group of diseases characterized by an uncontrolled growth of abnormal cells which tend to proliferate in an uncontrolled way. The term 'cancer' represents numerous disease types, depending on the type of cell from which the tumor emanates. This, along with the grade of tumor maturity determines its ability to grow, invade adjacent tissues, and spread throughout the body.

Cancer diseases represent a serious public health problem since they affect many people and are a frequent cause of death. According to a worldwide statistics from the "World cancer report 2008", there were 12.4 million new cancer cases diagnosed and 7.6 million deaths reported from the disease in 2008 [1].
The 5-year relative survival rate for all cancers diagnosed between 2001 and 2007 is 67%, up from 49% in 1975-1977. The improvement in survival reflects both progress in diagnosing certain cancers at an earlier stage and improvements in treatment [2].

Tumor spread, type, and differentiation are generally the most important factors for determining the prognosis and choice of treatment [3]. Treatments for cancer include surgery, chemotherapy, radiotherapy, hormonal therapies and biological therapies. Treatment can be given with the aim of curing the cancer, controlling it or relieving symptoms.

People are often given more than one type of treatment for their cancer. Radiotherapy is commonly used as an essential component in the management of cancer patients, either alone or in combination with surgery or chemotherapy. This treatment modality is often given with the aim of destroying a tumor and curing the cancer (curative or radical radiotherapy), or when it's not possible to cure a cancer, radiotherapy may be given to relieve symptoms such as pain (palliative treatment).

The chance of tumor eradication with radiation depends on tumor-related factors, such as radio-sensitivity, volume, location and dissemination path, as well as factors related to the irradiation modality, such as the treatment plan and targeting accuracy. Higher doses of radiation generally give improved local control and possibly longer disease-free survival, but it is important to ensure that the radiation tolerance of adjacent normal tissues is not exceeded.

In the quest for ways to improve radiotherapy effectiveness, new approaches have been explored. Intensity-modulated radiation therapy, hadrontherapy and synchrotron radiation therapies are some examples.

Within this contest, spatially fractionated radiotherapy techniques are potentially able to spare normal tissues along with giving large amount of dose at the target.

In this work, Monte Carlo simulation of the dose deposition for two types of spatially radiotherapy techniques, Minibeam Radiation Therapy (MBRT) and Grid therapy, have been performed. The two techniques combine submillimetric field sizes and spatial fractionation of the dose. The resulting biological effects appear to

challenge many of the current paradigms in radiation therapy. Remarkable healthy tissue resistance to very high doses in one fraction was observed in several biological investigations performed during the last two decades. Other than x-rays radiation therapy techniques, other methods are available or in development, such as hadrontherapy which is an advanced external RT technique that uses charged particles. Particle beams have physical and radiobiological characteristics which differ markedly from those of conventional radiotherapy beams composed of γ-rays or x-rays: charged hadrons interact more readily with matter (have enhanced ballistic selectivity) allowing well-defined distribution of the dose in depth; while ions deposit a large fraction of their energy at the end of their track, resulting in intense local ionization that is considered highly effective against radiation-resistant tumors.

Using particle beams instead of x-rays, the ballistic properties of charged particles and their increased biological efficiency are added to the advantages of spatially fractionated techniques.

The MBRT potential to achieve high degrees of tumor control with less invasive effects on the surrounding healthy tissues, and the properties of hadrontherapy, are discussed in Chapter 1.

A brief introduction to radiobiology, which is fundamental to understanding the biological advantages of the use of hadrons, is provided in Chapter 2.

To perform Monte Carlo simulation, the GATE code was used. The description of the physics and the Monte Carlo code used, are given in Chapter 3.

The results obtained for MBRT with carbon and oxygen are presented in Chapter 4 and 5 respectively. On those chapters, all the data and calculations performed, are shown. The results related to carbon and oxygen are compared in Chapter 6.

The last chapter is devoted to simulations and their results in grid therapy implemented with protons.

Chapter 1

Principles of spatially fractionated radiotherapy

Contents

1.1 Radiotherapy: an overview

Radiotherapy, or radiation therapy (RT), is the treatment of cancer and other diseases with ionizing radiation. Ionizing radiation deposits energy that injures or destroys cells by damaging their DNA, thus making it impossible for them to reproduce. Radiation therapy can damage normal cells as well as cancer cells. Therefore, treatment must be carefully planned to minimize side effects. This is one of the greatest challenges of radiotherapy: to minimize damage to normal cells through the delivery of an adequate dose aimed to destroy tumor cells and spare their normal counterparts.

X-rays, gamma rays and charged particles are types of radiation used for cancer treatment. The radiation may be delivered by a machine outside the body (external-beam radiation) pointing the part of the body to be treated after the careful planning of where the generated beams will deposit their energy. Radiotherapy can also be given internally by drinking a liquid isotope, delivering it by intravenous injection or by placing a radioactive implant directly into or close to a tumor (internal radiation therapy, also called brachytherapy). The type of radiation therapy to use depends on the type and size of cancer, on his location, how close the cancer is to normal tissues that are sensitive to radiation, and how far into the body the radiation needs to travel.

Conventional external beam radiation therapy is used in the 80% of the cases and is delivered, for the most, using linear accelerator machines. Depending on the machine specifications, the energy can be varied with a range of 4-25 MV [4].

In order to reduce the side effects of the treatment, a selective tumor destruction can be achieved enhancing the precision in dose delivery. Different special techniques have been developed with this aim, between others:

- Three dimensional conformal radiotherapy (3-D CRT);
- Intensity modulated radiation therapy (IMRT);
- Image guided radiation therapy (IGRT);
- Respiratory gated radiation therapy;
- Adaptive radiotherapy;
- Stereotactic radiation therapy.

One of the most common types of external-beam radiation therapy is called 3-dimensional conformal radiation therapy (3D-CRT). Conformal radiotherapy uses a device called a multi-leaf collimator, which allows the beam of radiation to be shaped very precisely so that less healthy tissue is included in the therapy field. As a result, the healthy surrounding cells and nearby structures receive a lower dose of radiation, so the possibility of side effects is reduced.

At the same way, intensity modulated radiation therapy (IMRT) also uses multi-leaf collimator. During the treatment, parts of the multi-leaf collimator are moved. This enables to vary the intensity of the beam during the treatment.

In image guided radiotherapy (IGRT), 3-D scans are regularly taken during the treatment, so imaging tools interface with the radiation delivery system through hardware or software, and allow physicians to optimize the accuracy and precision of the radiotherapy by adjusting the radiation beam based on the true position of the target tumor and critical organs. This type of treatment can work well for tumors in areas of the body that may move during treatment, for example due to breathing [5].

Another radiotherapy technique that takes into account the body mouvement due to the breathing is the so called respiratory gated radiation therapy. Essentially, in this technique, the linac adapts to the patients breathing pattern, switching the beam off when the tumor moves outside the planned treatment volume and switching it back on when it comes back into position [6].

A new technique that compensates for changes in the location of the disease and normal tissue during the treatment is the adaptive radiotherapy (ART). This novel approach corrects for daily tumor and normal tissue variations through a systematic feedback of measurements [7].

Stereotactic radiation therapy is a specialized type of external beam radiation therapy. The term stereotactic refers to precise positioning of the target volume within three-dimensional (3D) space. There are two types of stereotactic radiation:

stereotactic body radiation therapy and stereotactic radiosurgery. The term body is used to distinguish the technique from the current terminology of stereotactic radiosurgery used for radiation treatment of central nervous system lesions. Stereotactic positioning can be precise, and as a result, stereotactic radiotherapy commonly uses higher doses per fraction and fewer fractions (hypofractionation) than conventional radiation [8].

1.2 Microbeam and Minibeam Radiation Therapy

The fundamental limitation of conventional radiotherapy is the risk of long-term damage to healthy tissue. To spare normal tissue and improve radiation treatment, different techniques have been conceived, as already discussed in previous section. In this context, spatially fractionated radiotherapies are included.

Spatially fractionated radiotherapy techniques such as:

- Microbeam radiation therapy (MRT);
- Minibeam radiation therapy (MBRT).

are an innovative method to spare healthy tissue.

MRT was initiated at the X17B1 superconducting wiggler beamline of National Synchrotron Light Source (NSLS), Brookhaven National Laboratory (BNL) around 1990 [9] [10], and then later developed at the European Synchrotron Radiation Facility (ESRF, Grenoble, France) since the mid-1990s [11] [12].
MRT is a spatially fractionated radiotherapy that uses an array of microscopically thin (25 to 100 μm width) and nearly parallel synchrotron-generated X-ray beams separated by 100 to 200 μm center-to-center distances [9]. The high flux of synchrotron light allows very high rates of dose deposition (several hundreds Gy within less than 1 s).
The properties of microbeams that make them a good candidate for tumor therapy are its outstanding sparing effect in healthy tissue, including the central nervous system (CNS) [13], and their preferential damage to tumors, even when administered from a single direction ([14], [15], [16], [17], [18], [19], [20]).

The biological basis of the healthy tissue sparing effect after MRT irradiation is not well understood. This effect was attributed to the rapid regeneration of the tissue's microvessels from cells surviving outside the microbeams' direct paths (for microbeam arrays, this means survival in the "valley" dose regions, i.e., the spaces between individual microbeams) [17]. This sparing effect vanishes when the valley dose approaches the tissue tolerance limit. Therefore, the damage threshold from MRT seemed to depend mostly on the valley dose [15].

The preferential tumoricidal effect of microbeams is thought to be partly due to the failure of the tumor's microvessels to repair the damage inflicted by these beams, which could then lead to the loss of blood perfusion and tissue necrosis ([15], [21],

[22]). The effects might reflect major differences between the microvasculature of normal tissues and tumors in response to radiation ([23], [24]), including the rapid proliferation of endothelial cells in tumors which may render their microvessels more vulnerable to microbeam damage, and the abnormal basement membrane in the tumor's vasculature [24].

The normal-tissue sparing effect of single-fraction microbeam arrays was established in the brain of the adult rat and in the cerebellum of suckling rats ([15], [17], [18], [20], [21], [25]), the CNS of duck embryos [14], the cerebellum of piglets [19], and the skin of the mouse [22] and the rat [26].

Despite MRT potential, a main drawback of this technique is the requirement of high photon fluxes that prevents artifacts caused by cardiosynchronous pulsations. Such high-intensity microbeams can only be produced by a synchrotron radiation source, which is a practical limitation for clinical implementation. Besides, microbeams require low-energy beams (<200 keV median energy), thus limiting dose penetration to the tissue. The reason is that if the range in the tissue of the photoelectrons and Compton electrons set in motion by incident photons is much larger than the thickness of the microbeams, the nearly rectangular-shaped dose distribution produced by each microbeam will develop broad shoulders that fill in the dose in the valley regions of the dose distribution (i.e., the regions between the direct microbeams to which radiation leaks). Furthermore, the clinical implementation of the interlaced method producing an homogeneous dose in the tumor is not possible in MRT due to the higher technical precision required.

Therefore, following the principle of spatial fractionation, an extension of the MRT method has been proposed by Dilmanian [27] from the National Synchrotron Light Source (Brookhaven National Laboratory, USA): the Minibeam Radiation Therapy.
In MBRT, the beam thickness ranges from 500 to 700 μm with a separation between two adjacent minibeams of the same magnitude. Thicker beams used in MBRT overcome the difficulties on the MRT implementation. Since the MBRT dose profiles are not as vulnerable as those of MRT to beam smearing from cardiac pulsations, high dose rates are not needed. In addition, the use of higher beam energies is feasible in MBRT ($\geq$ 200 keV); this results in lower entrance doses to deposit the same integral dose in the tumor, despite the larger penumbral doses [28] [29].

The first experiments in MBRT were performed by Dilmanian at BNL. Rat spinal cords were irradiated with four 680 μm wide minibeams with a spacing of 4 mm. Despite the fact that some healthy tissue damage was observed, an entrance dose of 400 Gy was tolerated in three out of four rats, as opposed to what happened in seamless beam irradiations. In addition, MBRT irradiations (680 μm wide minibeams spaced by 1360 μm) of rat brains showed a 4-fold higher tolerance with respect to broad beams, founding an equivalent tissue tolerance to that previously found in MRT [27], [30].

The use of MBRT is also being explored at the ESRF [28], where studies in

white-beam have shown a gain factor of three in the mean survival time of 9L gliosarcoma bearing-rats with respect to controls [31]. Another study, conducted at ESRF, demonstrates the sparing effect of minibeams on healthy tissue and shows the feasibility of using X-ray minibeams with high doses in brain tumor radiotherapy [32].

1.2.1 Peak-to-Valley dose ratio

In MBRT irradiation, the resulting dose profiles consist of a pattern of peaks and valleys, with high doses along the minibeam path and low doses in the spaces between them. The minimum dose in the central region between two microbeams is named the valley dose and the dose at the centre of the microbeam is the peak dose (Fig. 1.1).

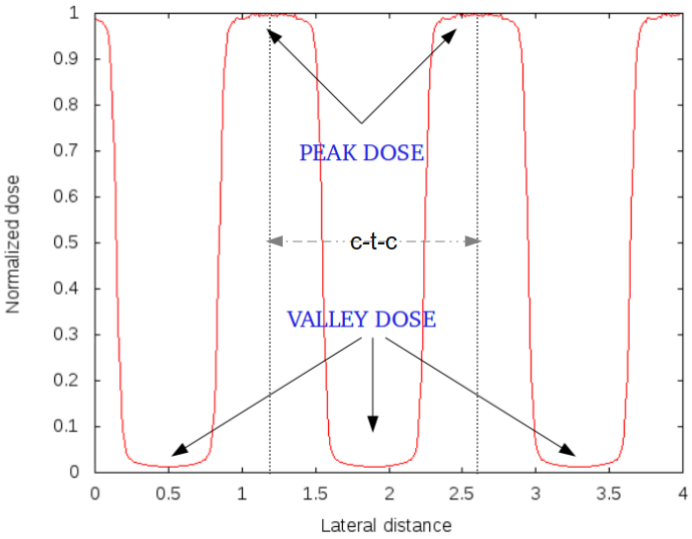

Figure 1.1: *Example of a lateral array dose profile. Peaks and valleys regions are pointed out.*

The separation between the centers of two consecutive peaks is called center-to-center distance (c-t-c). The ratio between the peak dose and the valley dose is called PVDR (peak-to-valley dose ratio).
PVDR is an important dosimetric parameter in spatially fractioned techniques, since it plays an important role in biological response. The PVDR depends on the incident beam energy, beam width, c-t-c distance, irradiation field size and tissue composition. PVDR should be as higher as possible in normal tissues and as closer to 1 as possible in tumor to ensure an homogeneous dose at the target.

1.3 Effectiveness of spatial fractionated radiotherapy

The smaller the field size is, the higher the tolerance of the healthy tissue: this phenomenon has been known since the 60s, when Zeman and collaborators investigated the possible hazards of heavy cosmic rays in the astronauts's brain [33],[34],[35]. They irradiated mice brains with 22.5 MeV deuteron beams of several field sizes and they evaluated the threshold dose to produce necrotic lesions along the first half of the beam path (1.5 mm) within 24 days. The reconstruction of the results is represented in figure 1.2. The tolerance doses remain almost constant for field sizes

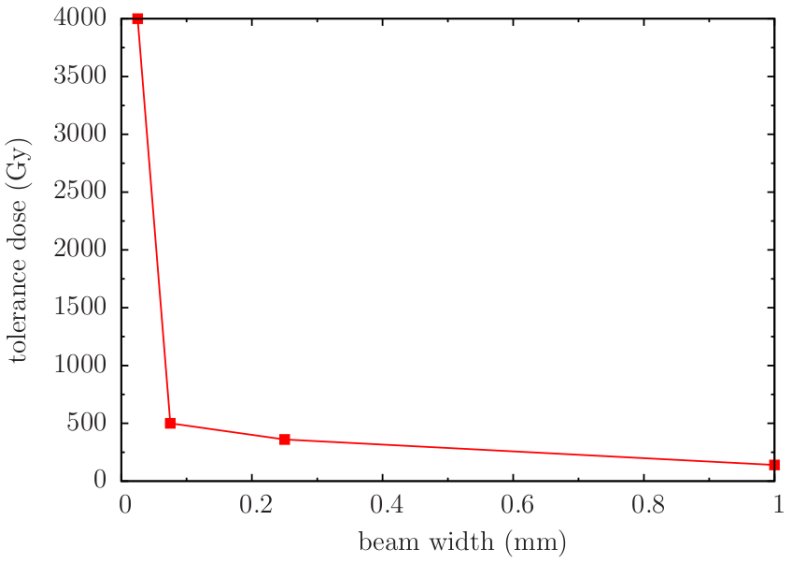

Figure 1.2: *Tolerance doses (in Gy) of mice brains to irradiation with 22.5 MeV deuteron beams of several widths (mm). There is an inverse relationship between radiosensitivity and volume of tissue exposed for small volumes. This is known as the dose-volume effect [33].*

larger than approximately 0.1 mm; below this value, the tolerance dose increases drastically.

Figure 1.3 shows histology images of mice brains irradiated with 22.5 MeV deuteron beams. The image on the left-hand side refers to an irradiation with a beam diameter of 1 mm and entrance dose of 280 Gy, while the right-hand side image shows the effect of a microbeam 25 μm diameter and a much higher dose of 4000 Gy. The paths of the beams are shown as dotted lines. For the irradiation with the microbeam the tissue is well preserved despite the high dose. For the millimetric irradiation beam, 240 Gy is enough to completely destroy the tissue.

This result clearly indicate that there is an inverse relationship for small volumes between radiosensitivity and volume of tissue exposed.

The dose-volume effect might be explained by the stem cell depletion hypothesis [36]: for each organ, there is a critical volume that can be repopulated by a single

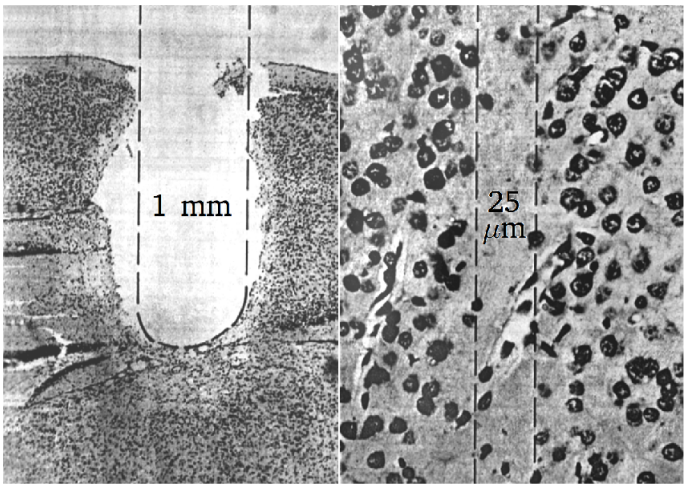

Figure 1.3: *Histology images of mice brains illustrating the dose-volume effect. On the left, complete tissue destruction is observed after irradiation with a 22.5 MeV deuteron beam of 1 mm of diameter and an entrance dose of 280 Gy. On the right, the tissue is well preserved after irradiation with a 25 μm wide beam and an entrance dose of 4000 Gy [34].*

survival stem cell that migrates from the nearby tissue to recover the tissue damaged by the radiation. Thus, the combination of submillimetric field sizes and spatial fractionation of the dose provides a further gain in tissue sparing due to the biological repair of the microscopic lesions by the minimally irradiated contiguous cells.

So the possible improvement of spatially fractionated radiotherapy, is the superior normal tissue tolerances, allowing the use of higher and potentially curative doses.

1.4 Hadrontherapy

Other than x-rays radiation therapy techniques, other methods are available or in development, such as hadrontherapy which is an advanced external RT technique that uses charged particles such as protons, alphas, C, O, etc.

By contrast with X-rays or γ-rays, which are absorbed by the body and show an exponential decrease in the radiation dose with increasing tissue depth, charged particles instead are characterized by a relatively low dose at the shallow depths, a peak near the end of the range, and then a rapid fall-off (Fig.1.4). The peak occurs immediately before the particles come to rest and is called the Bragg peak, for William Henry Bragg who discovered it in 1903.

The idea is to deliver a high dose of ionizing radiation to a deep seated tumor while not exceeding the tolerance dose of the intervening normal tissues, and no dose will be given to normal tissues beyond the tumor.

Wilson was the first to point out the advantageous dose distributions of protons

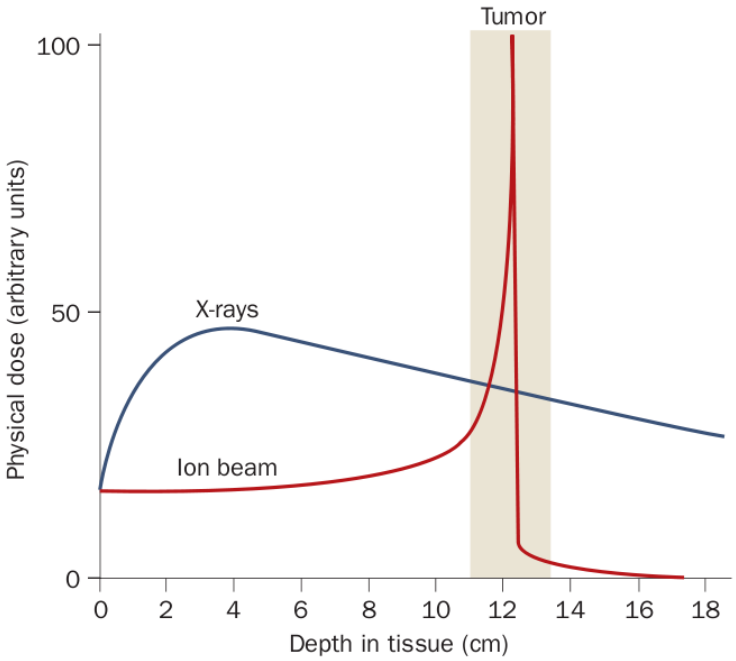

Figure 1.4: *Comparison of the depth dose relationships for X-rays and high-energy charged particles [37].*

and their potential for cancer therapy.

Since the Bragg peak for particles of a given energy is very narrow, beams of different energies have to be superimposed to produce a spread-out Bragg peak (SOBP) that covers the whole tumor (Fig.1.5).

A SOBP can be produced in two possible ways: a beam of particles with a fixed energy can be attenuated with range shifters of variable thickness, which produces Bragg curves that peak at different depths along the tumors (passive modulation). Alternatively, the energy of the particle beam can be varied in the accelerator, and in this case no passive attenuators are needed (active modulation).

Always Wilson proposed for first, the use of range modulation wheels for producing spread-out Bragg peaks that cover larger targets that can be treated with pristine Bragg peaks.

The first proton treatment of human patients was carried out by Tobias, Lawrence and others on the LBL cyclotron in the late 1950s.

In 1958, Larson and Leksel reported the first use of range modulation to form a SOBP and beam scanning to produce large treatment fields in the lateral dimension.

From the late 1960s until 1980, there were significant efforts in the development of proton therapy at several physics research facilities around the world. Proton therapy programs were initiated in Russia and in Japan. Between 1980 and 2000,

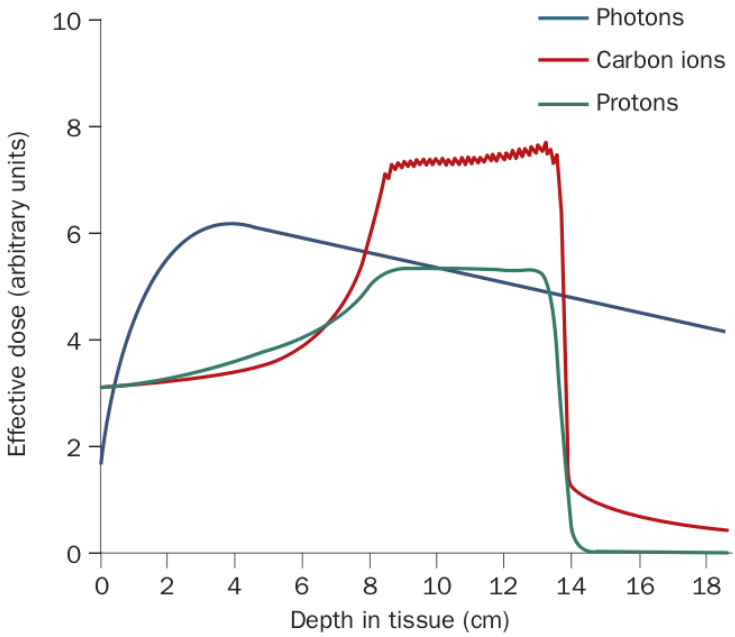

Figure 1.5: *Example of SOBP [37].*

there was a flurry of activity in proton therapy around the world, with patients treatment starting in England, France, South Africa, Switzerland, Germany, Japan and Russia.

In 1975, Cornelius A. Tobias proposed that particles heavier than protons could give additional advantages. In fact, heavy ions have reduced lateral scattering compared with protons, which leads to a further improvement in the dose distribution to the target area. The main potential advantages of heavy ions, however, are in their radiobiological effects on tissues. The relative biological effectiveness (RBE; that is, the ratio of X-ray and particle dose producing the same biological effect) of charged particles is increased by increasing the particle ionization density, or linear energy transfer (LET). The LET depends on the charge and velocity of the ion: fast moving, light ions have low LET, and their biological effectiveness is close to that of X-rays; slow, heavy ions have high LET, and are more effective than X-rays for killing cells, as well as for other end points, such as causing mutations.

Most of the clinical experience with ions heavier than protons involves carbon, because this particle has an RBE of about 1 in the entrance channel and as high as 3-4 in the Bragg peak region. Ions heavier than carbon are difficult to use for therapy, first because the nuclear fragmentation of the projectile unfavorably modifies the shape of the Bragg curves, and second because LET is already high in the entrance channel. Oxygen can be used in special cases; for example, very hypoxic tumors. On the other hand, ions with mass between those of protons and carbon (from ^{4}He to ^{10}B) could also have applications in therapy. The physical and radiobiological basis of the action of energetic charged particles suggest that the use of protons can

represent a technical improvement for conformal therapy, and heavy ions a potential breakthrough for the treatment of radiotherapy-resistant cancers such as renal-cell carcinoma, melanoma and glioblastoma [37].

1.4.1 Hadrontherapy facilities in Europe

Hadrontherapy is today part of the medical business landscape, several companies are focusing their work, not only in protontherapy centers, but also on carbon therapy facilities.

As already explained, the concentration of energy deposition of ions in a localized Bragg peak gives a better ballistic precision compared to photons, so a better preservation of the healthy tissues and organ at risk in the tumor vicinity.
Concerning the ballistic precision, carbon ions have the disadvantage of dose deposition after the Bragg peak due to the ion fragmentation. Nevertheless, this drawback is largely compensated by a much lower radial diffraction, a diffraction which penalizes protons for the treatment of deep-seated tumors.
The decisive advantage of ions compared to photons and protons comes from their higher LET and RBE, that is why a major attention is now focused on the development of carbon therapy.
In this paragraph, some of the hadrontherapy facilities in Europe are presented [38].

GSI, Germany: with HIMAC in Japan, GSI is the place where a decisive pioneer work has been done for carbon therapy. First of all, here, has been done the research works on the RBE of the ions and the links between RBE and DNA damages, repairing and non-repairing cells. The "Local-Effect-Model" (cell survival) has been built and verified making in-vitro and in-vivo experiments. Finally, the RBE modelling has been validated and a Treatment Planning System (TPS) has been constructed. GSI makes also decisive technical developments to improve the quality of the treatments. The most famous is the raster scanning (spot-scanning) technique which allows a nearly perfect dose deposition in the tumor with an optimal preservation of the surrounding tissues.

HIT Heidelberg, Germany: the work done at GSI has lead to the construction of a dedicated heavy ion therapy center at Heidelberg. The accelerator started to work in 2007. This facility is equipped with 3 treatment areas, and it can work with p, He, C, O ions in a range energy 50-430 $MeV/nucleon$.

CNAO, Pavia, Italy: the realization of the Italian National Center for Oncological Hadrontherapy (CNAO) started in 2002. The basic design of the accelerator and beam lines comes from the Proton-Ion Medical Machine Study (PIMMS) done at CERN. This carbon facility is equipped with 3 treatment rooms and a room for QA and experimental researches.

1.4.2 Carbon therapy facilities around the world

Carbon therapy facilities in operation:

	Country	Energy (MeV)	Start	Tot. patients	at date
HIMAC, Chiba	Japan	800/u	1994	6569	Dec-11
HIBMC, Hyogo	Japan	320/u	2002	788	Dec-11
HIT, Heidelberg	Germany	430/u	2009	980	Dec-12
GHMC, Gunma	Japan	400/u	2010	271	Dec-11
IMP-CAS, Lanzhou	China	400/u	2006	159	Dec-11
CNAO, Pavia	Italy	430/u	2011	0	Nov-12

Carbon therapy facilities in a planning stage or under construction:

	Country	Energy (MeV)	No. rooms	Start planned
Med-AUSTRON, Wiener Neustadt	Austria	430/u	3	2015
Fudan University, Shanghai	China	430/u	3	2014
PTC, Marburg	Germany	430/u	4	2012?

All those data, are published on the Particle Therapy Co-Operative Group (PTCOG) website:
http://ptcog.web.psi.ch/

1.5 Combination of spatially fractionated techniques and hadrontherapy

The aim of this work is to study the possible feasibility of an heavy ion treatment with arrays of minibeams.

The new technique will take advantages on the sparing of normal tissue from the spatially fractionated method and from the better ballistic of heavy ion therapy, and a gain, from the radiobiological point of view, will be add thanks to the RBE characteristic of heavy ions.

Chapter 2

Introduction to radiobiology

Contents

Radiobiology is a branch of science concerned with the action of ionizing radiation on biological tissues and living organisms. Knowledge of the radiobiology of normal tissues and tumors is a core prerequisite for understanding the main difference between x-ray radiation therapy and hadrontherapy.

The biological effects of irradiation are the end product of a long series of phenomena which are set in motion by the passage of radiation through the medium. The initial events are ionizations and excitations of atoms and molecules of the medium along the tracks of the ionizing particles. These physical perturbations lead to physico-chemical reactions, then chemical reactions and finally the biological effect [39].

Ionizing radiation may be divided into directly and indirectly ionizing for the understanding of biological effects. Most of the particulate types of radiation are directly ionizing as they can directly break up the atomic structure of the absorbing medium through which they pass producing chemical and biological damage to molecules. In contrast, electromagnetic radiations, namely, X and γ rays, are indirectly ionizing because they do not produce chemical and biological damage themselves but produce secondary electrons after energy absorption in the material.

The biological effects of radiation result principally from damage to DNA, which is the critical target. If any form of radiation is absorbed in biological material, there is a possibility that it will interact directly with the critical targets in the cells. The atoms of the target itself may be ionized or excited, thus initiating the chain of events that leads to a biologic change. This is called direct action of radiation and it is the dominant process if radiations when high linear energy transfer (LET) is considered.

Alternatively, the radiation may interact with other atoms or molecules in the cell (particularly water) to produce free radicals that are able to diffuse far enough to reach and damage the critical targets. This is called indirect action of radiation [40].

2.1 Linear energy transfer

When ionizing radiations traverse through matter, they lose energy gradually through various interaction processes along the length of their path. For a particular absorber, the rate of loss of energy depends on the energy and type of radiation as well as the density of the material.
The density of energy deposition in a material is called the Linear Energy Transfer (LET) of the radiation. It is defined as the average energy deposited per unit length of track of radiation and the unit is $keV/\mu m$.

LET essentially indicates the quality of different types of radiation and is important because the biological effect of a radiation (its relative biological effectiveness, RBE) depends on its average LET.

Radiations are categorized into low and high LET, with charged particles radiations usually being high LET radiations (because of their greater energy deposition along the track) whereas X and γ rays are low LET radiations due to their sparse ionizations. As the charged particle deposits energy in a tissue, it slows down. Due to this fact, the LET varies along the path of these particles, while the energy transfer rate ($-dE/dX$, loss of energy per unit distance) increases. This is shown by a peak of energy deposition at the end of the track (the Bragg peak).

Energy loss events are essentially randomly distributed along the track of the photon or charged particle. For low LET radiations the energy deposition events along the track of the photon are sparse relative to the dimensions of biomolecules such as DNA, with the result that photons may pass through such a molecule without depositing any energy. For such radiations the amount of energy deposited in a region of the track similar in dimensions to biological molecules also varies widely from a few eV up to 100s of eV. For high LET radiation the energy loss events are much more closely spaced and a significant amount of energy will be deposited along all parts of the track similar in dimension to biomolecules. Typical LET values for various radiations are listed in table 2.1.

2.2 Chemical interactions

The physical interactions of ionizing radiation lead to loss of energy of radiation and production of ionization and excitation of atoms and molecules which may convert into free radicals in pico to femto seconds after physical interaction with atoms ($10^{-13\ to\ -15}$ s).

Typical LET values of ionizing radiation	
Radiation LET	$keV/\mu m$
Co-60 γ rays	0.2
250 kVp X-rays	2.0
10 MeV protons	4.7
150 MeV protons	0.5
14 MeV neutrons	12
2.5 MeV α particles	166
2 GeV Fe ions	1000

Table 2.1: Hall and Giaccia, [40]

Hereafter, it is schematized the process conducting from the physical interaction to the biological effects:

Ionizing radiation
↓
Fast electron
↓
Ion radical
↓
Free radical
↓
Chemical changes from the breakage of bonds
↓
Biological effects

A free radical is an atom or molecule carrying an unpaired orbital electron in the outer shell.
In an atom or molecule with an even number of electrons, spins are paired: this state is associated with a high degree of chemical stability. In an atom or molecule with an odd number of electrons, there is one electron in the outer orbit for which there is no other electron with an opposing spin; this is an unpaired electron. This state is associated with a high degree of chemical reactivity.

Radiation interactions that produce biologic changes are classified as either direct or indirect. The change takes place by direct action if a biological macromolecule such as DNA, RNA, or protein becomes ionized or excited by an ionizing particle or photon passing through or near it. Indirect effects are the result of radiation interactions within the medium (e.g. citoplasm) which create reactive chemical species that in turn interact with the target molecule (see picture 2.1).
Because 70% to 85% of the mass of living systems is composed of water, the vast majority of radiation-induced damage is mediated through indirect action on water molecules.

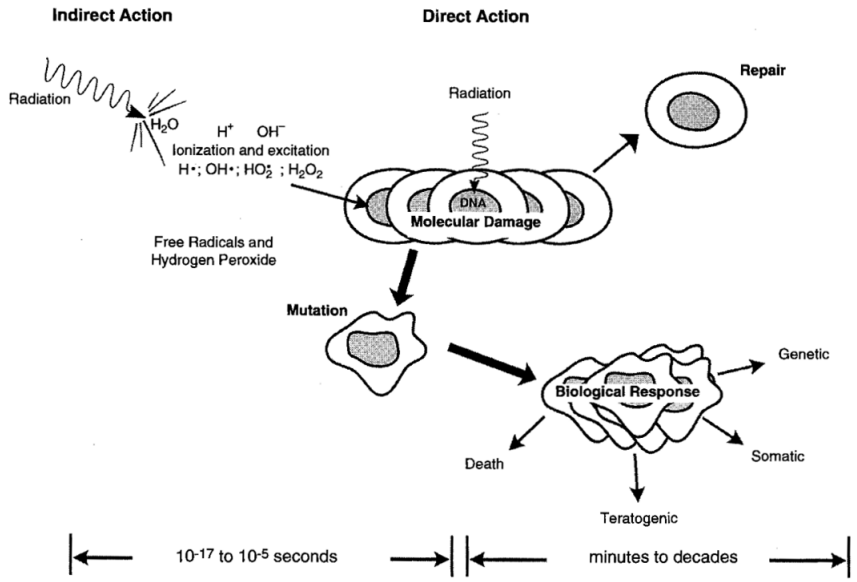

Figure 2.1: *Direct and indirect actions [41]*

The absorption of radiation by a water molecule results in an ion pair (H_2O^+, H_2O^-). The H_2O^+ ion is produced by the ionization of H_2O, whereas the H_2O^- ion is produced via capture of a free electron by a water molecule.
These ions are very unstable; each dissociates to form another ion and a free radical:

$$H_2O^+ \rightarrow H^+ + OH\bullet$$

$$H_2O^- \rightarrow H\bullet + OH^-$$

The H^+ and OH^- ions do not typically produce significant biologic damage because of their extremely short lifetimes ($\approx 10^{-10} sec$) and their tendency to recombine to form water.
Free radicals are extremely reactive chemical species that can undergo a variety of chemical reactions. Free radicals can combine with other free radicals to form nonreactive chemical species such as water (e.g., $H\bullet + OH\bullet = H_2O$), in which case no biologic damage occurs, or with each other to form other molecules such as hydrogen peroxide (e.g., $OH\bullet + OH\bullet = H_2O_2$), which are highly toxic to the cell.
Free radicals can act as strong oxidizing or reducing agents by combining directly with macromolecules. The damaging effect of free radicals is enhanced by the presence of oxygen. Oxygen stabilizes free radicals and reduces the probability of free radical recombination to form water. Oxygen combines with the hydrogen radical to form the highly reactive hydroperoxyl radical (e.g., $H\bullet + O_2 = HO_2\bullet$).

Although their lifetimes are limited (less than 10^{-5} sec), free radicals can diffuse in the cell, producing damage at locations remote from their origin. Free radicals may inactivate cellular mechanisms directly or via damage to genetic material (DNA

and RNA), and they are believed to be the primary cause of biological damage from low LET radiation.

2.3 Radiation lesions in DNA

Cells contain numerous macromolecules, only some of which are essential for cell survival. If a key molecule, for which the cell has not replacement (e.g. DNA), is damaged or destroyed, the result may be cell death. There is considerable evidence that damage to DNA is the primary cause of radiation-induced cell death.

Radiation causes a wide range of lesions in DNA such as single-strand breaks, double-strand breaks (in which both strands of the double helix break simultaneously at approximately the same nucleotide pair), base loss, or base changes (see figure 2.2).

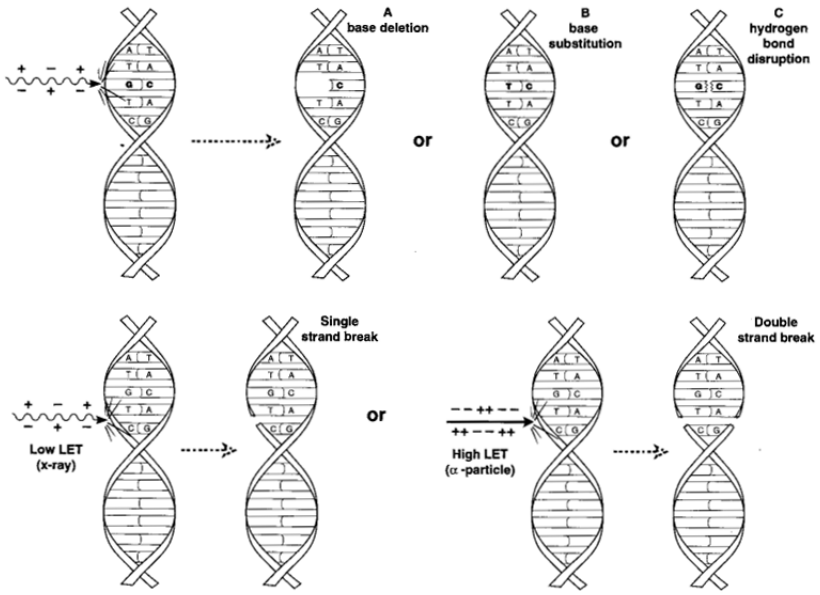

Figure 2.2: *Examples of DNA mutations. [41]*

The number of DNA lesions generated by irradiation is large, but the number giving rise to cell kill is extremely small [42]. The numbers of lesions induced in the DNA of a cell by a dose of 1-2 Gy from photon radiation are approximately:

Double-strand breaks play a critical role in cell killing, and there are experimental data showing initially-produced double-strand breaks correlate with radiosensitivity and survival at low dose, and unrepaired or mis-repaired double-strand breaks to correlate with survival after higher doses. Increasing evidence suggests the importance of complex double-strand breaks lesions after high LET irradiation.
The single-strand breaks are more easily repaired than double-strand breaks and

Events per 1-2 Gy dose	
Ionization	≈ 100000/cell
Base damage	> 1000/cell
Single strand breaks	≈ 1000/cell
Double strand breaks	≈ 40/cell
Cell deaths	≈ 0.63/cell

Table 2.2: Frequency of DNA damage from photon radiation, [42]

are more likely to result from the sparse ionization pattern that is characteristic of low-LET radiation.

Knowledge of radiation track structure has been used to explain the wide variation and wide distribution of lesions in DNA. The importance of clusters of energy deposition events (ionizations and excitations) at track termini of secondary electrons resulting in multiple closely-spaced lesions (multiply damaged sites) within a range of 20 nm, has been recognized as crucial for cell killing and for the ability of cells to repair such lesions.

Different repair pathways are used to repair DNA damage, depending on the stage of the cell cycle. If the damage is not repaired before DNA synthesis, the lesion may be transmitted during mitosis and meiosis. Chromosomal damage that occurs before DNA replication is referred to as chromosome aberrations, whereas that occurring after DNA synthesis is called chromatid aberrations. Unlike chromosomal aberrations, only one of the daughter cells will be affected if only one of the chromatids of a pair is damaged.

Aberrant chromosomes arise when broken ends rejoin with other broken ends to generate rings, dicentrics, translocations and other chromosome aberrations. Dicentric chromosome aberrations arise post replication from the joining of 2 broken chromatids in different chromosomes and can be used as a marker for radiation exposure. Acentric fragments and dicentrics are unstable aberrations and may not survive past the next mitosis, implicating loss of genetic material which may signal death in diploid cells.

2.4 Cell cycle and cell death

Cells are the unit that make up tissues. They contain inorganic compounds (water and minerals) as well as organic compounds (proteins, carbohydrates, nucleic acids and lipids).
The two main constituents of a cell are the cytoplasm, which supports all metabolic functions within the cell, and the nucleus, which contains the genetic information (DNA).

The cell proliferation cycle is divided in four periods: G1, S, G2, M.
S is the period of DNA synthesis and M stands for mitosis, where division takes place. The S and M portions of the cell cycle are separated by the two periods

G1 and G2 when, respectively, DNA has not yet been synthetized or has been synthetized but other metabolic processes are taking place.

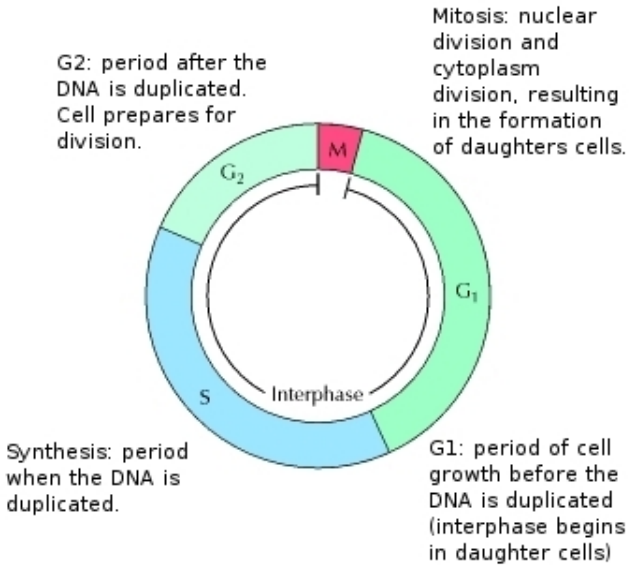

Figure 2.3: *Schematic representation of the cell cycle [40].*

In general, cells are most radiosensitive in the M and G2 phases, and most resistant in the late S phase [40].

The cell cycle time of malignant cells is shorter than that of some normal tissue cells, but during regeneration after injury normal cells can proliferate faster. Cell death of non-proliferating cells is defined as the loss of a specific function, while for stem cells and other cells capable of many divisions it is defined as the loss of reproductive integrity. A surviving cell that maintains its reproductive integrity and proliferates almost indefinitely is said to be clonogenic.

Irradiation of a cell will result in one of the following nine possible outcomes:

- no effect;
- division delay: the cell is delayed from going through division;
- apoptosis: the cell dies before it can divide or afterwards by fragmentation into smaller bodies, which are taken up by neighbouring cells;
- reproductive failure: the cell dies when attempting the first or subsequent mitosis;
- genomic instability: there is a delayed form of reproductive failure as a result of induced genomic instability;
- mutation: the cell survives but contains a mutation;

- transformation: the cell survives but the mutation leads to a transformed phenotype and possibly carcinogenesis;
- bystander effects: an irradiated cell can send signals to neighbouring unirradiated cells and induce genetic damage in them;
- adaptive response: the irradiated cell is stimulated to react and become more resistant to subsequent irradiation.

The timescale involved between the breakage of chemical bonds and the biological effect may be hours to years, depending on the type of damage. If cell kill is the result, it may happen in hours to days, when the damaged cell attempts to divide (early effect of radiation); this can result in early tissue reactions if many cells are killed. If the damage is oncogenic, then its expression may be delayed for years (late effect of radiation) [4].

In general, the radiation sensitivity of a tissue is proportional to the rate of proliferation of its cells and inversely proportional to the degree of cell differentiation.

For example, the following tissues and organs are listed from most radiosensitive to least radiosensitive:

Most sensitive:	blood-forming organs
	reproductive organs
	skin
	bone and teeth
	muscles
Least sensitive:	nervous system

Factors that make cells less radiosensitive are: removal of oxygen to create a hypoxic state, the addition of chemical radical scavengers, the use of low dose rates or multifractionated irradiation, and cells synchronized in the late S phase of the cell cycle [4].

2.5 Cell survival curves and therapeutic index

A cell survival curve depicts the relationship between the fraction of cells retaining their reproductive integrity and the absorbed dose.
Cell survival as a function of radiation dose is graphically depicted on a logarithmic scale, and is plotted on the y-axis against dose on the x-axis. Cell surviving fractions are determined with in vitro or in vivo techniques. Examples of survival curves for cells irradiated by densely and sparsely ionizing radiation beams are shown in figure 2.4.

The type of radiation influences the shape of the cell survival curve. Irradiation of cells with high-LET radiation produces linear survival curves on the log-linear plot. For low LET radiation, however, the curves show an initial slope followed by a shoulder region and then become nearly straight at higher doses.

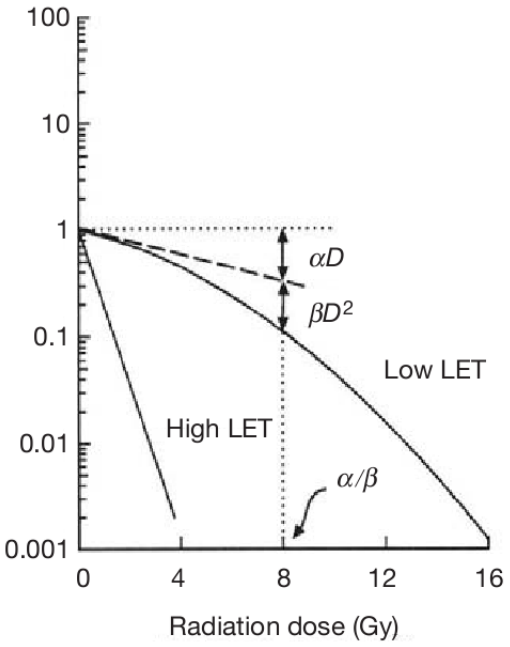

Figure 2.4: *Typical cell survival curves for densely ionizing radiation (high LET) and sparsely ionizing radiation (low LET) in the linear quadratic model [4].*

Several mathematic methods have been developed to define the shape of cell survival curves; nowadays, the most often used is the linear quadratic method:

$$S(D) = e^{-\alpha D - \beta D^2}$$

where:
$S(D)$ is the fraction of cells surviving a dose D;
α is a constant describing the initial slope of the cell survival curve;
β is a smaller constant describing the quadratic component of cell killing.
The ratio α/β gives the dose at which the linear and quadratic components of cell killing are equal.

It is also possible to define a dose response curve as a plot of a biological effect observed versus the dose given: with increasing radiation dose, radiation effects may increase in severity, in frequency, or both. Such dose response curves have a sigmoid shape, with the incidence tending to zero as dose tends to zero and the incidence tending to 100% at very large doses. This applies to both tumor control and normal tissue complications (Fig. 2.5).

The effects of radiation on tissue as a function of dose are measured with assays and the measurement results are given in the form of cell survival curves or dose response curves.

The ratio of the tumor response for a fixed level of normal tissue damage is called therapeutic index or therapeutic ratio. In the hypothetical example in figure 2.5, there is a favorable therapeutic index, because a 30% probability of tumor control

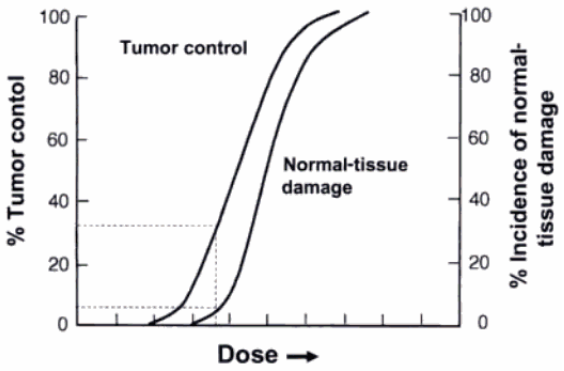

Figure 2.5: *Example of response curves. Tumor control probability and normal tissue complications are plotted as a function of dose. What is illustrated is a favorable situation where the tumor is more radiosensitive than the normal tissue [40].*

is possible for a 5% incidence of complications. The two sigmoid curves depicted on that figure are, one for the tumor control probability (TCP) and the other for the normal tissue complication probability (NTCP). The optimum choice of radiation dose delivery technique in the treatment of a given tumor is such that maximize the TCP and simultaneously minimizes the NTCP. For a typical good radiotherapy treatment, TCP$\geq$ 0.5 and NTCP$\leq$ 0.05. So the therapeutic index can also be defined as the ratio of the TCP and NTCP at a specified level of response (usually 0.05) for normal tissue.

The therapeutic index varies with many factors, such as the dose rate and LET, the presence of radiosensitizers or radioprotectors, the design of the treatment plan and the precision of implementation of the treatment plan. However, it is imperative that the average doses to normal tissues be kept lower than the doses to tumors in order to minimize treatment complications and optimize treatment outcomes. In modern radiotherapy this is achieved through sophisticated 3D treatment planning and dose delivery.

2.6 Relative biological effectiveness

Although all ionizing radiations are capable of producing the same types of biological effects, the magnitude of the effect per unit dose differs. Equal doses of radiation of different LETs do not produce the same biologic response. To evaluate the effectiveness of different types of radiations and their associated LETs, experiments are performed that compare the dose of the test radiation required to produce the same specific biologic response produced by a particular dose of a reference radiation (typically x-rays produced by a potential of 250 kVp).
The RBE relates the effectiveness of the test radiation to the reference radiation.

For identical exposure conditions, it is defined as follows:

$$RBE = \frac{\text{Dose of 250-kVp x-rays required to produce effect X}}{\text{Dose of test radiation required to produce effect X}}$$

RBE depends on the following:

- LET;
- radiation dose;
- number of dose fractions;
- dose rate;
- biological system or end point.

So, as stated before, radiation quality includes the type of radiation and its energy, whether electromagnetic or particulate, and whether charged or uncharged.

RBE depends on the dose level and the number of dose fractions (or, alternatively, the dose per fraction) because in general, the shape of the dose-response relationship varies for radiations that differ substantially in their LET.

RBE can vary with the dose rate because the slope of the dose-response curve for sparsely ionizing radiations, such as x- or γ-rays, varies critically with a changing dose rate. In contrast, the biologic response to densely ionizing radiation depends little on the rate at which the radiation is delivered.

The biologic system or the end point that is chosen has a marked influence on the RBE values obtained. In general, RBE values are high for tissues that accumulate and repair a great deal of sublethal damage and low for those that do not.

2.6.1 RBE as function of LET

As the LET increases, the RBE increases slowly at first and then more rapidly as the LET increases beyond 10 keV/μm. Between 10 and 100 keV/μm, the RBE increases rapidly with increasing LET and in fact reaches a maximum at about 100 keV/μm. Beyond this value for the LET, the RBE again falls to lower values.

Radiation with a LET of about $100keV/\mu m$ is optimal in terms of producing a biologic effect. At this density of ionization, the average separation between ionizing events coincides with the diameter of the DNA double helix ($\approx 2nm$). Radiation with this density of ionization has the highest probability of causing a double-strand break by the passage of a single charged particle.
In the case of x-rays, which are more sparsely ionizing, the probability of a single track causing a double-strand break is low, and in general more than one track is required. As a consequence, x-rays have a low biologic effectiveness.
At the other extreme, much more densely ionizing radiations (with a LET of $200keV/\mu m$) readily produce double-strand breaks, but energy is wasted because the ionizing events are too close together. Because RBE is the ratio of doses producing equal biologic effect, this more densely ionizing radiation has a lower RBE than the optimal

LET radiation. The more densely ionizing radiation is just as effective per track, but less effective per unit dose.

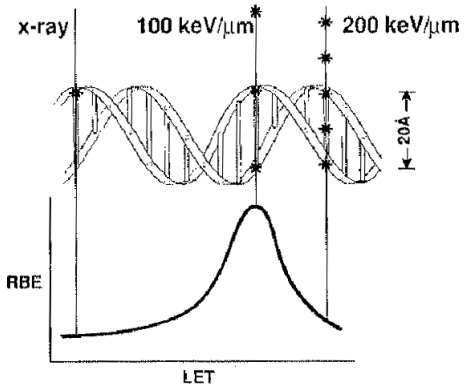

Figure 2.6: *The most biologically effective LET is that at which there is a coincidence between the diameter of the DNA helix and the average separation of ionizing events. [40]*

2.7 The oxygen effect and radiosensitivity

The presence or absence of oxygen within a cell influences the biological effect of ionizing radiation: the larger the cell oxygenation, the larger is the biological effect of ionizing radiation especially for low LET radiations [4]. As shown in figure 2.8, the effect is quite dramatic for low LET (sparsely ionizing) radiations, while for high LET (densely ionizing) radiations it is much less pronounced.

The ratio of doses without and with oxygen (hypoxic versus well oxygenated cells) to produce the same biological effect is called the oxygen enhancement ratio (OER):

$$OER = \frac{\text{Dose to produce a given effect without oxygen}}{\text{Dose to produce the same effect with oxygen}}$$

The OER decreases as the LET increases and approaches as shown in figure 2.9.

Cells at the periphery of tumour cords growing around blood vessels become chronically hypoxic because of the consumption of most of the oxygen near the blood vessel. The transient closing of blood vessels can also make the whole tumour cord hypoxic for a few minutes at a time. Reoxygenation is the process by which cells that are hypoxic become oxygenated after irradiation, through the killing and removal of oxic radiosensitive cells from the tumour.

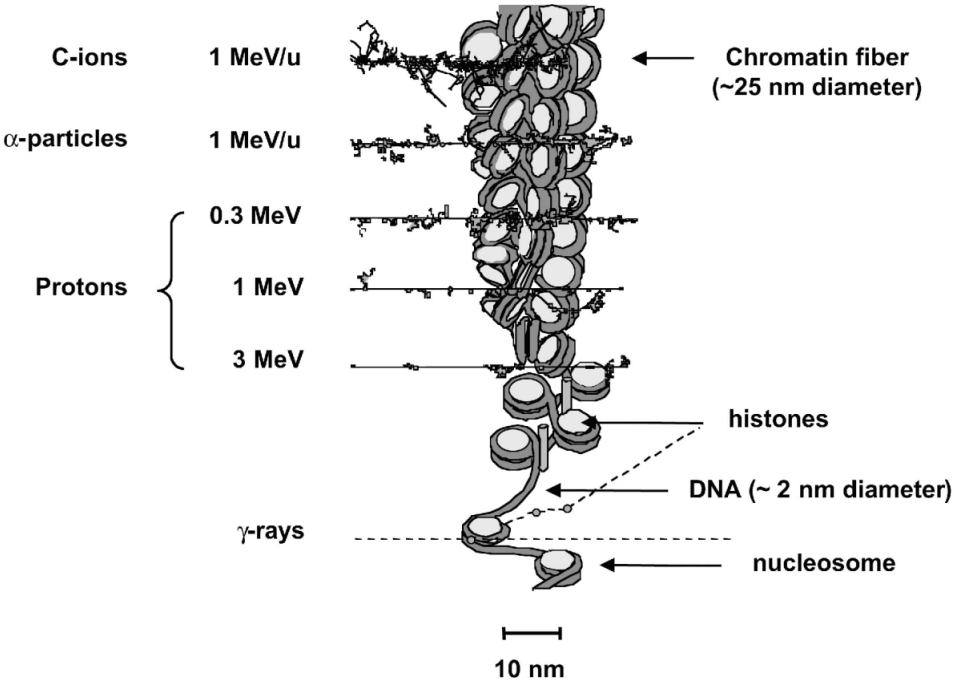

Figure 2.7: *Schematic representation of tracks of sparsely and densely ionizing radiations compared with relevant biological targets (chromatin fiber, nucleosomes and DNA double helix). [43]*

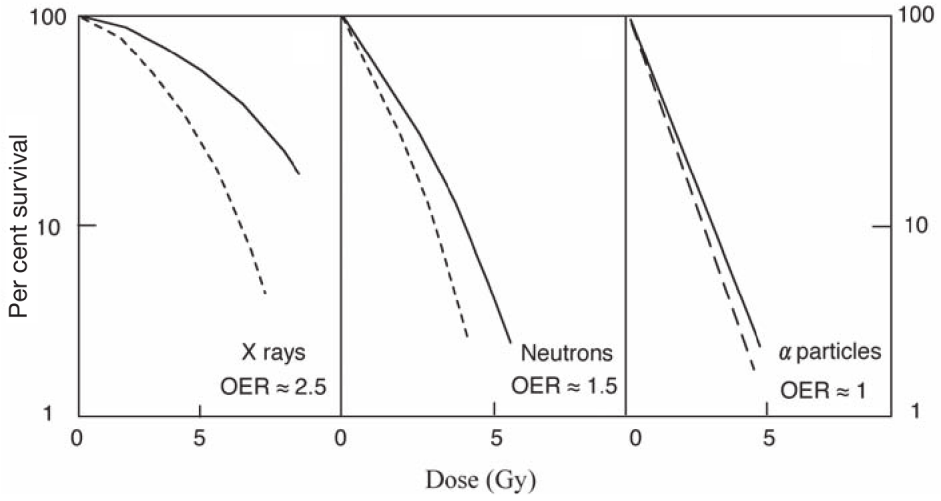

Figure 2.8: *Typical cell surviving fractions for X-rays, neutrons and α particles: dashed curves are for well oxygenated cells, solid curves for hypoxic cells. [4]*

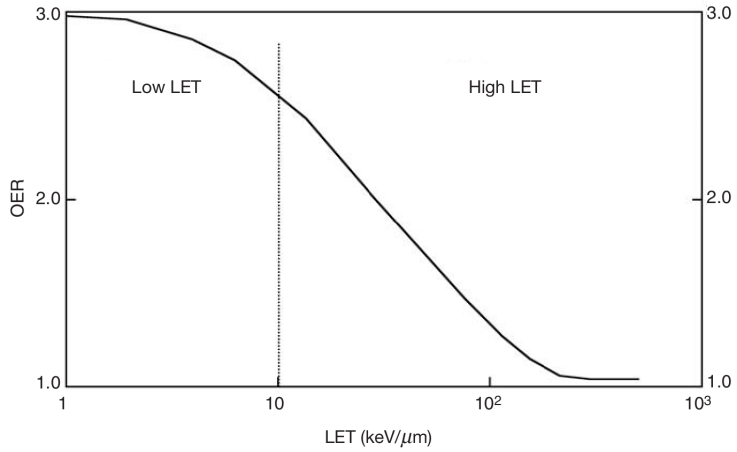

Figure 2.9: *OER plotted against LET. The vertical dashed line separates the low LET region, where LET* $< 10keV/\mu m$*, from the high LET region, where LET* $> 10keV/\mu m$*. [4]*

2.8 Radiobiological motivation for hadrontherapy

The particle or hadron beams deployed in radiotherapy (protons, neutrons and helium, carbon, oxygen and neon ions) have a physical and radiobiological characteristics which differ from those of conventional radiotherapy beams (photons) and which offer a number of theoretical advantages over conventional radiotherapy. The main potential advantages of heavy ions are in their radiobiological effects on tissues. The RBE of charged particles is increased by increasing the particle ionization density (LET).

The LET depends on the charge and velocity of the ion: fast moving, light ions have low LET, and their biological effectiveness is close to that of X-rays; slow, heavy ions have high LET, and are more effective than X-rays for killing cells, as well as for other end points, such as causing mutations.

As an example, carbon ions at an energy of 300 MeV per nucleon have a range in water around 20 cm, and can be used to treat deep tumors. The LET of such ions is low (around 10 $keV/\mu m$) in the entrance channel, where normal tissue is exposed, and high (around 50-80 $keV/\mu m$) in the Bragg peak region, where the tumor is located. As a result, the biological effects of treatment with these ions in normal tissue are comparable to those seen with X-rays (and, therefore, normal tissue complications are similar to those expected in conventional treatment); however, cell killing is enhanced in the tumor region.

High LET (densely ionizing) radiation has several other radiobiological advantages compared to X-rays. Cells are well known to have increased sensitivity to X-rays in the presence of oxygen, but the oxygen enhancement ratio is reduced at high LET values, with the result that hypoxic tumors have increased sensitivity to heavy ions. The cell-cycle dependence of cell killing, as well as the cell-sparing effect

of fractionation, are also reduced in the Bragg peak region, which further enhances the effectiveness of particle therapy in the tumor compared to the normal tissue.

Chapter 3

Materials and Methods

Contents

On this chapter, the Monte Carlo code GATE, used for the simulations, has been described in particular focusing on the phantom, the source and the readout parameters.
The physics list has also an extremely significant role in the simulations. So the physics for hadrons interactions in matter will be briefly described and so its implementation in the code.

3.1 The Monte Carlo method

The name "Monte Carlo" was coined in the 1940s by scientists working on the nuclear weapon project in Los Alamos, to designate a class of numerical methods based on the use of random numbers.
The Monte Carlo method is a statistical approach of deriving a macroscopic solution to a problem by the use of random numbers. It involves the random sampling of probability distribution functions that describe the problem of interest. Provided that the algorithm is accurate and the physical system is well modeled, repeated sampling of the distributions will converge to the correct solution.

Monte Carlo methods usually follow different approaches, depending on the particular field of application. However, these approaches tend to follow a particular scheme: define a domain of possible inputs, generate inputs randomly from the domain using a certain specified probability distribution, perform a deterministic

computation using the inputs and aggregate the results of the individual computations into the final result. Thus, the reliance computation is sensitively dependent on the goodness of the random numbers, which are required in large amounts to achieve good statistics. This requirement led to the necessity of using methods which in some a way are able to "create" long chain of random numbers, giving rise to the development of the so called pseudorandom[1] numbers generators.

Nowadays, Monte Carlo methods are widely used to solve complex physical and mathematical problems ([51]), they are especially useful to study systems with a large number of coupled degrees of freedom, such as fluids, disordered materials, strongly coupled solids, and cells.
In the Monte Carlo simulation of radiation transport, particles travel in discrete steps and undergo various types of interactions along the way. The history of a particle is viewed as a random sequence of free flights that end with an interaction event where the particle changes its direction of movement, loses energy and, occasionally, produces secondary particles. The step length and the type of interaction are sampled from cross section data. Sampling of the appropriate differential cross sections, random histories can be generated and so energy and direction of the resultant particles can be determined.

The integral parts of the code include: the cross section data of the processes to be simulated, the particle transport algorithms, the specifications of the geometries and quantities to be scored, as well as the analysis of the simulation.

3.2 The GATE simulation toolkit

Monte Carlo simulation is a essential tool in nuclear medicine. Accurate and versatile simulation codes such as GEANT3/4, EGS4, MCNP/MCNPX, PENELOPE, FLUKA, they all include well-validated physics models, geometry modeling tools, and efficient visualization utilities. However these packages are quite complex and necessitate a steep learning curve.

GATE is an advanced opensource software developed by the international OpenGATE collaboration and dedicated to numerical simulations in medical imaging and radiotherapy. It currently supports simulations of Emission Tomography (Positron Emission Tomography - PET and Single Photon Emission Computed Tomography - SPECT), Computed Tomography (CT) and Radiotherapy experiments. Using an easy-to-learn macro mechanism to configurate simple or highly sophisticated experimental settings, GATE now plays a key role in the design of new medical imaging devices, in the optimization of acquisition protocols and in the development and

[1] A pseudorandom number generator is an algorithm for generating a sequence of numbers that approximates the properties of random numbers. The sequence is not truly random in the sense that it is completely determined by an initial state, usually named seed. When Monte Carlo simulations are exploited to produce a unique result by splitting the process in several tasks, the use of different seeds is mandatory.

assessment of image reconstruction algorithms and correction techniques. It can also be used for dose calculation in radiotherapy experiments.

Gate is a GEANT4 application that encapsulates the GEANT4 libraries in order to achieve a modular, versatile, scripted simulation toolkit adapted to the field of nuclear medicine.

Here, a brief description of the code is presented. A general simulation architecture for dosimetry and radiotherapy applications follows:

- define the source;
- define the phantom geometry;
- specify the output;
- setting up the physics processes;

and then initialize the simulation.

3.2.1 Source

A source in GATE is defined by its:

- particle type (e.g. radionuclide, gamma, positrons, ions, etc);
- position (volume);
- direction (solid angle);
- energy (spectrum).

A source is represented by a volume in which the particles are emitted. The type of particle can be choose from a list of simple particles (e^-, e^+, γ, etc) or a ion source can be simulated defining its atomic number, atomic weight, ionic charge in units of energy and its excitation energy in keV.

Different types of source distribution can be defined: volume, point, beam, plane or surface, as well as its placement.

The angular distribution of the emission can also be defined. By default, a full span of 0-180 degrees for the polar angle and 0-360 degrees for the azimuthal angle are defined.

At last, the energy distribution can be expressed using a pre-defined spectrum or by using built-in distributions.

3.2.2 Phantom geometry

The definition of a geometry is a key step in designing a simulation. Particles are then tracked through the components of the geometry.

When a volume is created with GATE a shape has to be assigned to it. Different volume shapes are available, namely: box, sphere, cylinder, cone, hexagon, general

or extruded trapezoid, wedge and elliptical tube. After creating a volume with a shape, its dimensions are the default dimensions associated with that shape. These default dimensions can be modified.

A material must be associated with each volume. The default material assigned to a new volume is air. The primary method for defining the properties of the materials used in Gate is by a materials database. This file holds all the information required for Gate to assign the nuclear properties from the Geant4 data sets, and is easily modified by the user. The material database contains two Geant4 structures called elements and materials that are used to define the physical properties of the atoms, molecules, and compounds. In contrast with Geant4, Gate does not use isotopic abundances. Elements are the building blocks of all the materials used in Gate simulations. Elements in Gate are defined as in a periodic table. Gate stores the elements name, symbol, atomic number, and molar mass. In Gate, materials are defined as combinations of elements, and are an important parameter that Gate uses for all of the particle interactions that take place during a simulation. These combinations of elements require defining four additional parameters. These are the material's name, density, constituent element(s), and their individual abundances.

In GATE, the parametrized volume method is available for voxelized phantoms. The parametrized volumes method offers several advantages such as: voxel that can be varied in size, shape and material, voxel not entirely filling the envelope, and visualization attributes.

In GATE, a compression algorithm is also implemented, in order to generate a compressed phantom where voxel size is variable; all adjacent voxels of the same material are fused together to form the largest possible rectangular voxel. A compressed phantom uses less memory and also less CPU.

3.2.3 Readout parameters

Actors are tools which allow to interact with the simulation. There are different types of actors which collect different types of information, such as energy deposit, number of particles created in a given volume, etc.

Some actors, such as the dose actor, can store some information into a 3D rectangular image (or matrix) according to the spatial position of the hit. User can specify the resolution of the 3D matrix (in this case, the size is equal to the size of the bounding box of the attached volume). Alternatively, user can specify the size to allow larger of smaller matrices.

3.2.4 Physics setup

There is a wide set of physics models to handle the interactions of particles with matter across a very wide energy range. Physics models cover the physics of photons, electrons, muons, hadrons and ions.

Currently, the maximum energy used in a medical application is 5 GeV per particle. Thus, simulation of medical applications requires electromagnetic and

hadronic processes below 10 GeV.

Each process have a model which generates the final state and a cross-section which represents the probability of interaction (the cross-section is sometimes called dataset).

In GATE is possible to define a physics list specifying all the particles, physics processes and cut-off parameters.

3.3 Physical processes of interest in this work

Charged particles interact with a transversing medium through a large number of collisions with the atoms of the medium. These collisions can be either elastic, in which the involved particle momenta are conserved, or inelastic, where part of the momenta and energy is converted. For heavy particles, the effect of the elastic collisions is mainly a small deflection of the particle trajectory inducing a range and a lateral spreading, and the main physical process involved is the inelastic collision of nuclei on the electrons of atoms present in the target matter.
In that process, the projectile of kinetic energy E_e, looses an energy $\delta E = e_e + I$ where e_e is the energy of the out-coming electron and I the ionization potential of that electron.

The impinging particles transfer most of their energy via secondary electron production, so the emitted electrons, or $\delta - rays$, forms the core of the track around the particle trajectory.

For heavy ions, the most of the primary energy is deposited by collisions of primary, secondary, and later generations of electrons with target molecules. The rest of the energy is consumed in nuclear processes, like nuclear collisions and nuclear fragmentation, and excitation processes.

To compute the stopping power induced by many collisions on electrons, the Bethe-Bloch formula is used. A relativistic version of the Bethe-Bloch formula has been proposed by Fano:

$$\frac{dE}{dx} = \frac{a\pi e^4 Z_t z^2}{m_e v^2}\left[ln\left(\frac{2m_e v^2}{< I >}\right) - ln(1-\beta^2) - \beta^2 - \frac{C}{Z_t} - \frac{\delta}{2}\right] \tag{3.1}$$

where Z_t is the target atomic number, z is the projectile atomic number, e the electron charge, m_e the electron mass, v the projectile velocity, $\beta = v/c$ where c is the speed of light, C is a shell correction factor, δ a density effect correction and $< I >$ the mean ionization energy.

This last parameter is of crucial importance since it rules the energy loss of the projectile and its range. It can be estimated from the chemical formula of the material as follows:

$$ln(< I >) = \left(\sum_i \frac{\omega_i Z_i}{A_i} ln(I_i)\right) / \left(\sum_i \frac{\omega_i Z_i}{A_i}\right) \tag{3.2}$$

where:

- Z_i and A_i are the charge and mass numbers for element i;
- ω_i is the mass ration of element i in the material;
- I_i is the ionization energy of the element i.

It can be also determined from fits to experimental data. In this work, the $< I >= 75eV$ value for liquid water recommended by the ICRU, was used. A variation of $\Delta < I >= 5eV$ on the $< I >$ value leads to a variation of around 1 mm on the range.

According to the Bethe-Bloch formula, the rate of energy loss increases as the particle energy decreases; therefore, ionization density will increase along the particle path as it slows down. Near the end of the path, when most of its energy has been lost, dE/dx reaches a maximum, corresponding to the peak in energy loss at low energy,and then it drops to zero as the particle comes to rest. As already seen in previous chapter, this behavior is characteristic of the way charged particles distribute their energy in matter and it is called Bragg curve.

The elastic collisions with target nuclei and the Bremsstrahlung process are neglected for hadron therapy applications.

3.3.1 Energy, range and angular straggling

As the heavy ion beam loses energy, it broadens in a variety of ways including energy, position and angle.

For a beam of heavy ions, the Bragg peak spreads in energy and has a distinctive width. The width of the Bragg peak is caused by the summation of multiple scattering events that yield a Gaussian energy loss distribution often referred to as energy straggling [45] :

$$\frac{N(E)dE}{N} = \frac{1}{\alpha\pi^{1/2}} exp\left[-\frac{(E-\bar{E})^2}{\alpha^2}\right] \tag{3.3}$$

Energy straggling represents the specific number $N(E)$ of particles having energies in the range E to $E+dE$ divided by the number of particles N, with mean energy $\bar{E}$ after traversing a thickness x_0 of absorber. The distribution parameter or straggling parameter α is given by the expression [45] :

$$\alpha^2 = a\pi z^2 e^4 n Z x_0 \left[1 + \frac{KI}{mv^2} ln\left(\frac{2mv^2}{I}\right)\right] \tag{3.4}$$

where K is a constant depending on the electron shell structure of the absorber and Z is its atomic number.

In an analogous manner, the range straggling[2], expressed as the number of particles $N(R)$ with ranges R to $R+dR$ divided by the total number of particles of the same initial energy, is given by the equation [45] :

$$\frac{N(R)dR}{N} = \frac{1}{\alpha\pi^{1/2}} exp\left[-\frac{(R-\bar{R})^2}{\alpha^2}\right] \tag{3.5}$$

[2]The range of a charged particle is defined as the distance it travels before coming to rest.

where $\bar{R}$ is the mean range.

Upon entering a medium of thickness x_0, a collimated beam experiences multiple collisions that broaden the beam and cause it to diverge. This phenomena is called angle straggling, and the mean divergence angle $\bar{\theta}$ s given by [45] :

$$\bar{\theta^2} = \frac{2\pi z^2 e^4}{\bar{E}^2} n Z^2 x_0 ln\left(\frac{\bar{E} a_0}{z Z^{4/3} e^2}\right) \tag{3.6}$$

where a_0 is the Bohr radius:

$$a_0 = \frac{\hbar^2}{kme^2} \tag{3.7}$$

The relative range straggling is smaller for heavier particles and also the lateral spreading of the beam is smaller for heavy ions than the lateral spreading of protons.

3.4 Nucleus-nucleus collisions

When a heavy ion beam interacts with tissue, the interactions leave nuclei in an excited state, and these excited nuclei decay by a variety of processes including particle emission and deexcitation by photon emission. These secondary fragments must be considered in therapy dose planning because they broaden the Bragg peak; that is why nucleus-nucleus collisions play an important role in hadron therapy.

The nucleus-nucleus collisions can be schematically described by two steps: the first is called the “entrance channel phase“ and the second step is called the “decay phase“.

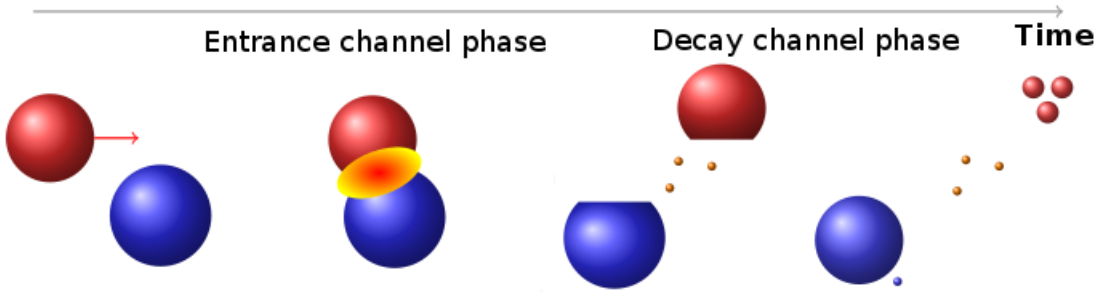

Figure 3.1: *Schematic representation of a nucleus-nucleus collision.*

The entrance channel phase is when a projectile hits a target nucleus and light particles are promptly emitted and an excited quasi-projectile and an excited quasi-target are formed. These excited nuclei decay through consecutive light particle emissions (”evaporation” process) or by a simultaneous break-up (“fragmentation“ process); this is the decay phase.

For both steps (schematically represented in figure 3.1), several models have been developed. A complete nucleus-nucleus collision modeling is achieved by a combination of a model describing the entrance channel and a model describing the decay phase.

Nucleus-nucleus collisions have two main effects. The first one is the disappearance of the projectile since the collision will change its nature. As a consequence, this projectile will not deposit its energy up to the Bragg Peak. The second effect is the secondary particle production. These fragments will be often of smaller size but with a velocity close to the velocity of the projectile. Because of the A/Z^2 scaling of the range for particles with the same velocity, these fragments will deposit their energy at penetration depths beyond the projectile Bragg Peak forming the so called "fragmentation tail".

In GATE, as in Geant4, three models are implemented for nucleus-nucleus collision:

- Abrasion-ablation model;
- Binary Light Ion Cascade model;
- Quantum Molecular Dynamic model.

The abrasion model is a simplified macroscopic model for nuclear-nuclear interactions based largely on geometric arguments rather than detailed consideration of nucleon-nucleon collisions. As such the speed of the simulation is found to be faster than models such as G4BinaryCascade, but at the cost of accuracy. By default, instead of performing an ablation process to simulate the de-excitation of the nuclear pre-fragments, the Geant4 implementation of the abrasion model makes use of existing and more detailed nuclear de-excitation models within Geant4 (G4Evaporation, G4FermiBreakup, G4StatMF) to perform this function. The abrasion interaction is the initial fast process in which the overlap region between the projectile and target nuclei is sheered-off. The spectator nucleons in the projectile are assumed to undergo little change in momentum, and likewise for the spectators in the target nucleus. Some of the nucleons in the overlap region do suffer a change in momentum, and are assumed to be part of the original nucleus which then undergoes de-excitation. Less central impacts give rise to an overlap region in which the nucleons can suffer significant momentum change, and zones in the projectile and target outside of the overlap where the nucleons are considered as spectators to the initial energetic interaction.
The initial description of the interaction must, however, take into consideration changes in the direction of the projectile and target nuclei due to Coulomb effects, which can then modify the distance of closest approach compared with the initial impact parameter. Such effects can be important for low-energy collisions.

The Geant4 Binary Cascade is an intranuclear cascade propagating primary and secondary particles in a nucleus. Interactions are between a primary or secondary particle and an individual nucleon of the nucleus, leading to the name Binary Cascade. In binary cascade model, each participating nucleon is seen as a Gaussian wave packet, and the total wave function of the nucleus is assumed to be direct product of these. This wave form have same structure as the classical Hamilton equations

and can be solved numerically. The Hamiltonian is calculated using simple time independent optical potential. Two nuclei are prepared according to this model and the lighter nucleus is selected to be the projectile. Nucleon in the projectile are entered with position and momenta into the initial collision state. Until first collision of each nucleon, its Fermi motion is neglected in tracking. Fermi motion and the nuclear field are taken into account in collision probabilities and final states of the collisions. Cross section data are used to select collisions. Where available, experimental cross sections are used by the simulation. The cascade terminates when the average and maximum energy of secondaries is below threshold. The remaining fragment is treated by precompound and de-excitation models.
However, binary cascade model, the Hamiltonian is calculated from the simple time-independent optical potential. A participant particle of the Binary Cascade is either a primary particle including nucleons in the projectile nucleus or particles generated or scattered in the cascade and only the participant particles are propagated in the nucleus. Furthermore, scattering between participant particles is not taken into account. This is one of the reasons that using the model for a heavy ion reaction, is not recommended.

Quantum Molecular Dynamics (QMD) [46] is the quantum extension of the classical molecular-dynamics model and is widely used to analyze various aspects of heavy ion reactions, especially for many-body processes, in particular the formation of complex fragments.
There are three major differences between Binary Cascade and QMD: the definition of a participant particle, the potential term in the Hamiltonian and the participant-participant interactions.

The entire nucleons in the target and projectile nucleus are considered as participant particles in the QMD model. Therefore each nucleon has its own wave function, however the total wave function of a system is still assumed as the direct product of them.

The potential terms of the Hamiltonian in QMD are calculated from the entire relation of particles in the system, in other words, it can be regarded as self-generating from the system configuration. On the contrary to Binary Cascade which tracks the participant particles sequentially, all particles in the system are tracked simultaneously in QMD. Along with the time evolution of the system, its potential is also dynamically changed. As there is no criterion between participant particle and others in QMD, participant-participant scatterings are naturally included. Therefore QMD accomplishes more detailed treatments of the above three points, however with a cost of computing performance.

3.5 Physics list

On this section, the physics list used to perform the simulation is presented.

The electromagnetic processes have been carried out by using the *StandardModel*

model, which has been widely validated and covers the range energy of interest for hadron therapy applications. This model implements a variety of electromagnetic processes for electron, positron, photon and charged hadrons interactions. The electron ionization is implemented; it calculates the energy loss due to ionization for electrons and positrons. The Bremsstrahlung energy loss contribution is calculated, as also the energy loss due to electromagnetic processes for hadrons. Finally, the MultipleScattering class simulates the multiple scattering of charged particles in material after a given step, then it computes the mean free path length correction and mean lateral displacement.

The hadronic processes are simulated using a generic elastic model for elastic hadron scattering. For the inelastic processes, the Binary Cascade model has been chosen for proton, and the QMD model has been chosen for ions.

For neutrons, the high precision inelastic and high precision capture models have been chosen. Those models generate the final state for neutron inelastic scattering and neutron capture using the high precision neutron model.

In table 3.1, the models used in the simulations for hadronic processes, are summarized.

	Hadronic processes		
	Particles	Geant4 processes	Geant4 models
Elastic scattering	GenericIon	G4HadronElasticProcess	G4LElastic
	all other particles	G4UHadronElasticProcess	G4HadronElastic
Inelastic process	Protons	G4ProtonInelasticProcess	G4BinaryCascade
Inelastic process	GenericIon	G4IonInelasticProcess	G4QMDReaction
Inelastic scattering	Neutron	G4NeutronInelasticProcess	G4NeutronHPInelastic

Table 3.1: Models used in the GEANT4 simulations.

3.6 Parameters as used on the simulations for this work

The geometry of the simulation has been built in GATE setting a world geometry as a cube 5 m per side.
The phantom is a cylinder of water with radius = 8 cm. Outside the cylinder the material is air.

The source has been set as a rectangular beam 0.70×10 mm with an energy Gaussian shape with 2 MeV σ. A beam divergency of 3 $mrad$ has been taken into account.

The dose map was collected by a parallelepiped DoseActor with dimensions $2 \times 2 \times 16$ cm. The 16 cm in depth were divided in 160 bins, with a voxel dimension in depth equal to 1 mm. The 2 cm along the lateral direction of the beam were divided in 2000 bins, with a voxel dimension, along the lateral direction, of 10 μm.

The number of showers was 10^7 for all the simulation.

Chapter 4

Carbon minibeam: simulations and results

Contents

In this Chapter, depth dose profiles and lateral dose profiles relating to a carbon minibeams array will be discussed.

A cylindrical water phantom has been utilized to simulate the irradiation, using planar sources of different energies. The computation of the absorbed dose is made by dividing the phantom's volume in voxels. Minibeam arrays have been simulated with the aid of superposition algorithms.

The peak to valley dose ratios have been evaluated for different center-to-center distances and configurations.

4.1 Introduction

As extensively discussed in previous chapters, the principle of MBRT is the dose-volume effect: the dose that biological tissues can tolerate is higher the greater the irradiated volume. By spatially dividing a single beam into an array of equally distant minibeams, the process of reconstruction of the damaged vasculature spreads from the tissue not directly irradiated to those in the beams' trajectories. The damage caused by the absorbed radiation is related to the absolute dose in the peak (i.e. along the beams' trajectories) and valley (between any two adjacent minibeams). Accurately evaluating these doses is an extremely important aspect of the therapy, and requires both direct (experimental) measures and their validation via Monte Carlo simulations.

Besides the dose-volume effect, the technique studied in this work, is aimed to achieve a high degree of conformity to the target volumes by exploiting the peculiar characteristics of the dose deposition due to the use of heavy ions. Indeed, heavy

ions offer an improved dose conformation as compared to photon and proton RT because of a sharp increase of dose in a well defined depth (Bragg peak) and a rapid fall-off beyond that maximum. In addition to a better sparing of normal tissue structures close to the target, heavy ions exhibit a strong increase of the LET in the Bragg peak as compare to the entrance region, with subsequent radiobiological advantages.

4.2 Simulation geometry and details

Because of the peculiarities of MBRT in terms of dose-rate and spatial fragmentation irradiation method, Monte Carlo simulations are particularly important in the development of the therapy.

The software described in Chapter 3, makes it possible to closely model the experimental configuration necessary to analyze the relationship between dose distributions and various parameters, such as the beams' energy and dimension, the distance between minibeams, the depth the beam can reach inside the irradiation volume, and the composition of the phantom.

The source used in the simulations reported in this chapter is represented by planar minibeam 700 μm wide and 2 cm high impinging on a water phantom as shown in figure 4.1. The phantom is a cylindrical volume 16 cm diameter and 16 cm long. The ideal area of the tumor is located after the center of the cylinder and it is represented by a parallelepiped 1 cm deep and square section 2 cm side.

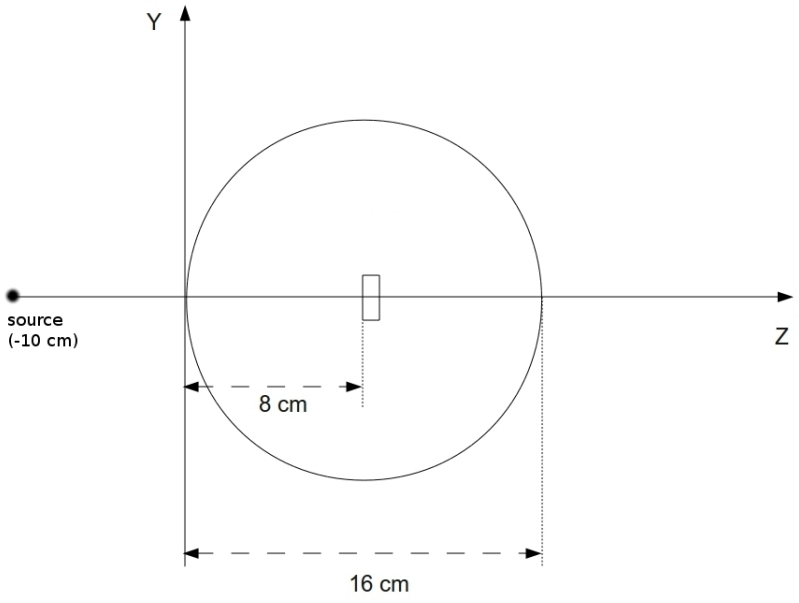

Figure 4.1: *In the simulations, a minibeam impinges on a water cylinder from the z-axis.*

Several monochromatic beams, with energies ranging from 195 to 205 $MeV/nucleon$,

have been simulated. For every energy value, a Gaussian spectrum with 2 MeV sigma, has been implemented. A divergence of the beam of 3 $mrad$ has been taken into account.

The goal is to cover the tumor volume using an array of minibeams. The array is obtained from a single minibeam using a superposition algorithm. In order to cover 2 cm, a certain number of beams need to be superimposed depending on the center to center (c-t-c) distance between two adjacent beams. In the next table, the number of beams in the array necessary to cover 2 cm, as a function of the c-t-c distance, are summarized.

Number of beams in an array	
c-t-c distance (μm)	# of beams
1400	15
2100	10
2800	8
3500	6

Table 4.1: Number of beams as function of the c-t-c distance

As an example, in figure 4.2, are shown a single lateral profile beam and the array lateral profile deriving from it.

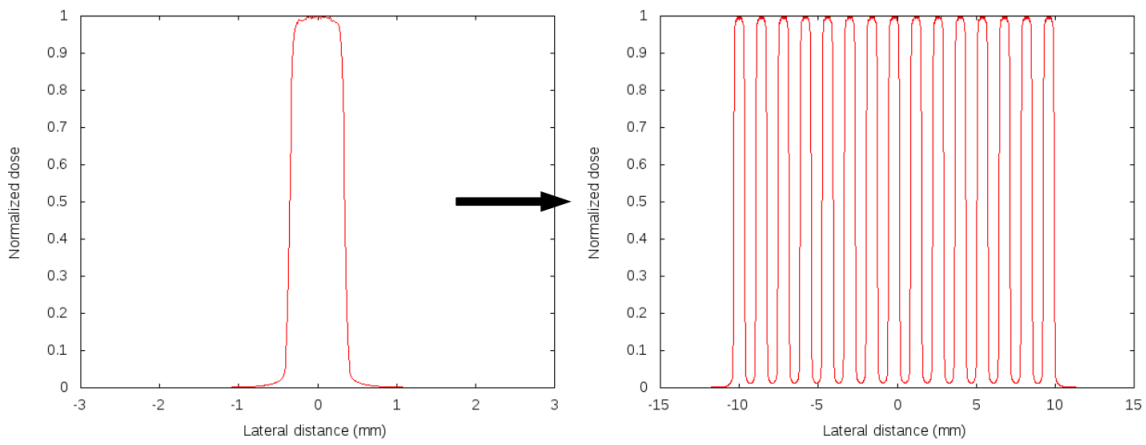

Figure 4.2: *Left panel: lateral profile of a 195 MeV/nucleon energy Carbon minibeam at 1 cm depth. Right panel: minibeams array for 195 MeV/nucleon energy Carbon minibeam at 1 cm depth and 1400 μm center-to-center distance.*

In building the array, the minibeams are superimposed one to each other, giving rise to the typical dose deposition profile characterized by peaks and valleys following each other.

4.3 Depth dose profiles for different energies

In figure 4.3 is shown the depth dose profile for a Carbon minibeam 195 $MeV/nucleon$. The Bragg peak is obtained at 8 cm depth. The dose deposited at 2 cm deep is about the 30% of the dose deposited at the Bragg peak, while the 50 % of the Bragg peak dose is reached very close to the Bragg peak itself.

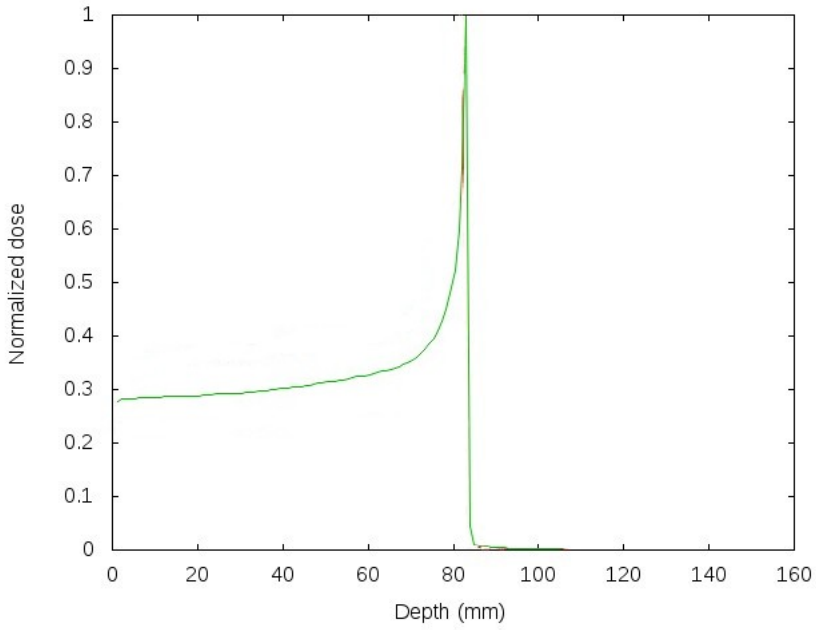

Figure 4.3: *Depth dose profile for a Carbon minibeam 195 MeV/nucleon*

In order to cover a certain distance in depth with the Bragg peaks, it is necessary to build a Spread Out Bragg Peak (SOBP). As already discussed in section 1.4, Chapter 1, the SOBP is the aggregate of several pristine Bragg peaks at staggered depths, and it can be obtained both in an active or passive way. Greater the energy, deeper Bragg peak is obtained.
The goal was to cover 1 cm of tissue starting from 8 cm in depth. So, several simulations have been performed changing the beam energy between 195 and 205 $MeV/nucleon$ with 1 $MeV/nucleon$ step. Each simulation consider a monchromatic beam. Adding together the data obtained with different beam' energies, the SOBP is obtained as in an active method.

In figure 4.4 are shown the depth dose distributions relating to different energy beams and the SOBP as a linear combination of these. A uniform region of dose is obtained between 8 and 9 cm. A flat physical dose at the SOBP is obtained by a weighted sum of the single monochromatic beams dose deposition: the lower energy beam should have a smaller weight because it leans on the plateau of dose due to the higher energies.

At 2 cm deep, the dose deposited is 41% of the dose at the Bragg peak. Also, the 50% of the Bragg peak dose is obtained at 5.5 cm. Those values are obviously higher

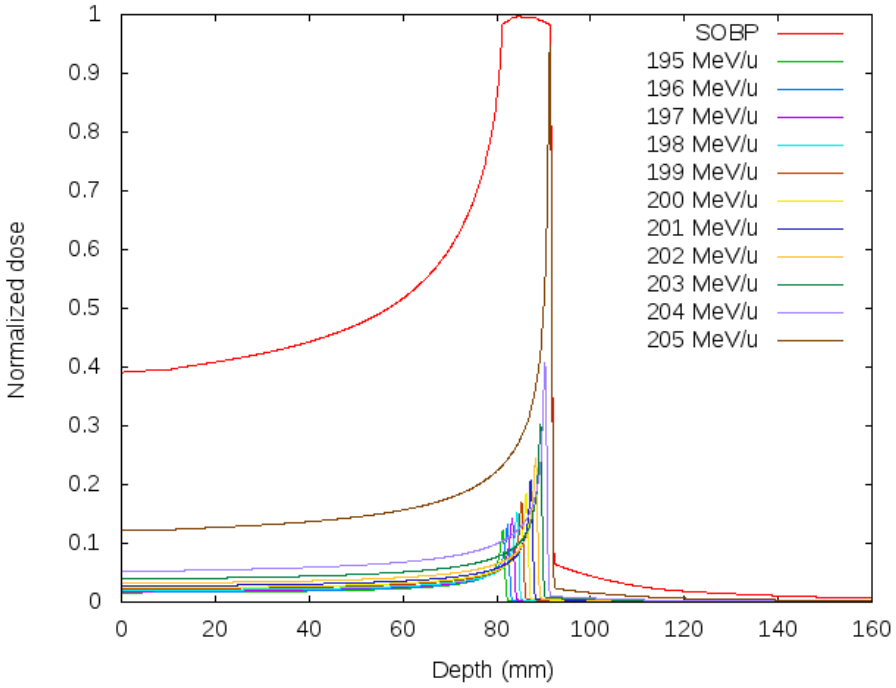

Figure 4.4: *SOBP obtained by a weighted sum of the Bragg peaks from different energies in the range between 195 and 205 MeV/nucleon.*

than the previous value for a single energy beam, but they are still reasonable. A good gain in the dose deposition, between the dose at the entrance and the dose at the Bragg peak, is obtained also with a SOBP:

195 *MeV/nucleon* monochromatic beam	3.4
Spread Out Bragg Peak	2.6

Table 4.2: Gain of dose at the Bragg peak respect to the entrance.

Furthermore, as observable in figure 4.4 and as explained in previous chapters, there is still a minor dose contribution behind the SOBP, which is due to lighter fragments produced in nuclear reactions of the carbon projectiles with the target material. This dose deposited is not negligible for the purposes of a treatment plan because it is due to elements of significant biological impact.

4.4 Lateral dose profiles

Heavy charged particles show a small angular scattering leading to sharp lateral boundary. This is of particular interest in the case of minibeams, because the lateral spreading of the beam influences the dose deposition in valley region and so the PVDR.

In figure 4.5 is shown a 3-D representation of the carbon minibeam path for 195 $MeV/nucleon$. X-axis represents the beam's path in depth and y-axis represents the lateral distance. At the beginning of the path, the lateral dimension of the beam is 0.7 mm, and it becomes much bigger at the Bragg peak because of the lateral spreading.

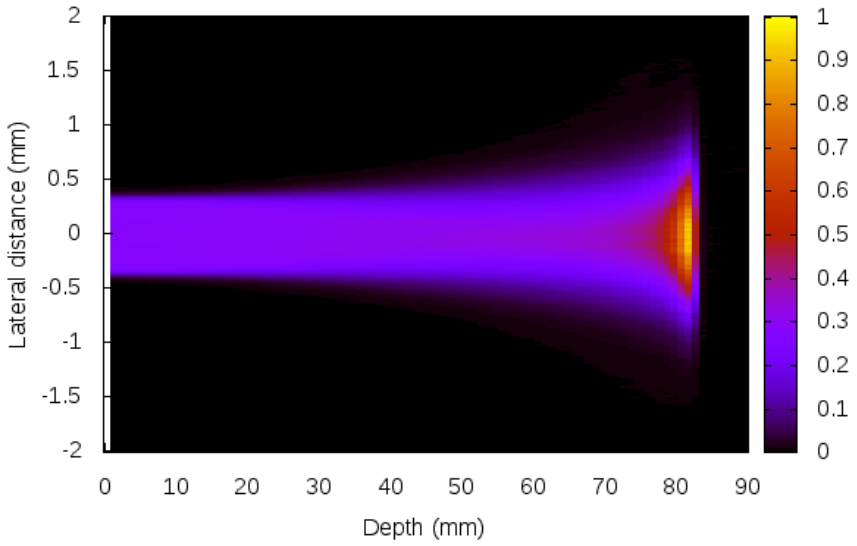

Figure 4.5: *Normalized depth dose deposition for a 195 MeV/nucleon Carbon minibeam in water.*

An alternative visualization is shown in figure 4.6, where the lateral profiles at different depths for a 195 $MeV/nucleon$ carbon minibeam are depicted. The data were sampled at 1, 3, 5, 7 and 8 cm depth. This plot highlights how greater the tails of the lateral distibution at deeper depths.

The dose in the valleys is strictly related to the extension of the tail in the lateral distribution of the beam. Studying the penumbra of the beams will explain the PVDR values discuss in next section.

Penumbra region is the rapid decrease at the edges of the radiation beam, and it is usually defined as the space between the 80% and 20% lateral dose profile.

In order to study the penumbra along the beam path, the positions on the lateral profile for the 80% and 20% (reported in figure 4.7) were recorded and compared.

The relative position of 20% regularly moves with increasing depth. This does not happen for the relative position to 80% of the dose. This is because, with increasing the depth, the initial shape of the beam is lost. The lateral profile of the beam, which originally was rectangular, gradually assume a Gaussian shape and that explains the particular trend. In any case, the distance between the position

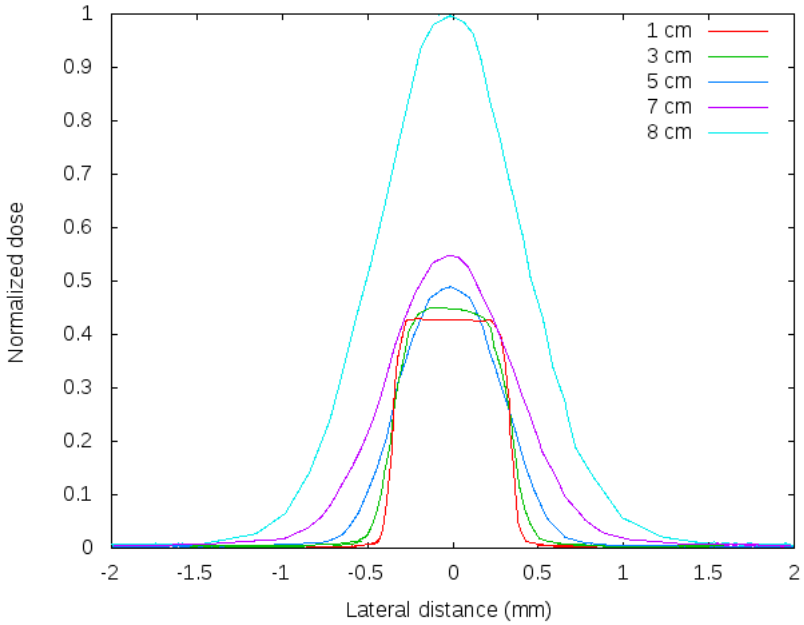

Figure 4.6: *Lateral dose distribution for a 195 MeV/nucleon carbon minibeam at 1, 3, 5, 7 and 8 cm depth.*

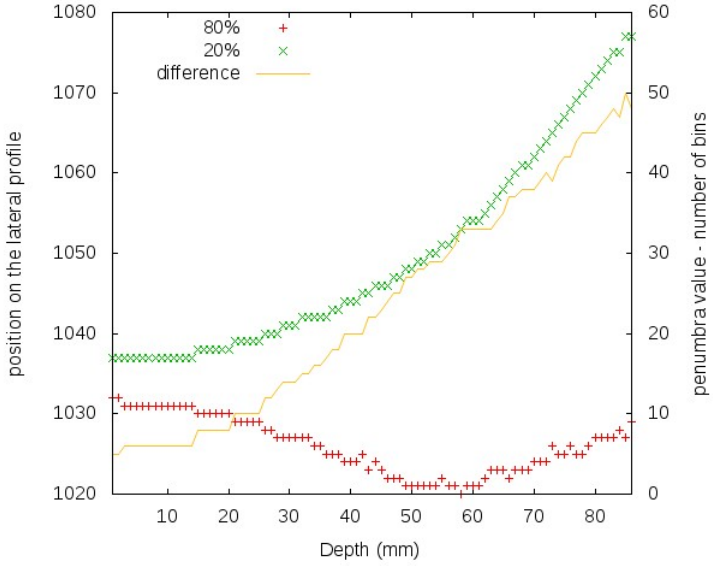

Figure 4.7: *In red, is the position of the point at* 80%*, and in green is the position of the point at* 20% *(first y axes). In yellow, is the difference between the previous abscissas, so the value of the penumbra in terms of number of bins (second y axes).*

for the 80% of the dose and those relating to 20%, i.e. the value of the penumbra for a given depth, is plotted in yellow, and denote the increase of the penumbra region in depth.

According to the geometry of the collection matrix, every bins of the lateral profile is $10\mu m$: the penumbra values in μm is obtained by a conversion of the number of bins, and it is reported in the next table.

Depth (cm)	Penumbra (μm)
1	60 ± 10
3	140 ± 10
5	280 ± 10
7	380 ± 10
8	450 ± 10

Table 4.3: Penumbra values along the beam path.

In the Spread Out Bragg Peak, all the energies contributes to the lateral dose profile. In figure 4.8 is shown a 3D representation of the dose distribution for the SOBP obtained using minibeams with energy ranging between 195 and 205 $MeV/nucleon$. On this new configuration, the volume covered by the Bragg peaks

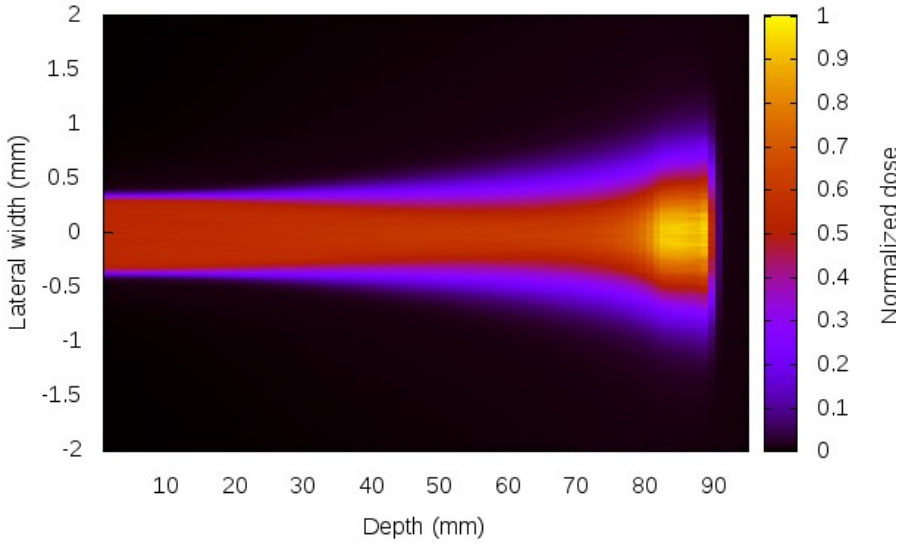

Figure 4.8: *Normalized depth dose deposition for minibeams with energy ranging between 195 and 205 $MeV/nucleon$.*

is 1 *cm* in depth, from 8 to 9 *cm*. A comparison between the 3D plot for the dose deposition in the case of a single beam (Fig. 4.5) and in the case of a SOBP (Fig. 4.8), shown a higher dose along the beam path for a SOBP, as already explained in the previous section.

Regard to the lateral spreading, any difference is noticeable between SOBP and monochromatic beam, until the Bragg peak region. Indeed, on that region, a slight widening is obtained between the lateral profile at 8 and 8.8 cm, as shown in figure 4.9

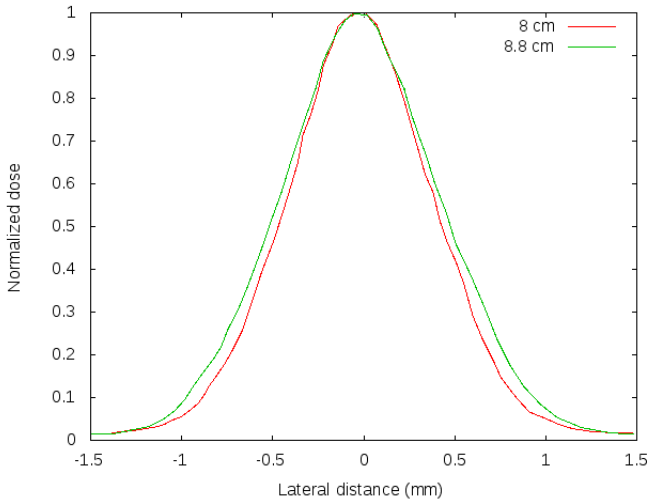

Figure 4.9: *Lateral distribution at 8 and 8.8 cm in the SOBP. A slight widening is obtained for the deepest position.*

4.5 Minibeams array and Peak to valley dose ratio

An array is obtained by overlapping minibeams. An algorithm, starting from the output data of the simulation, creates an array with a pre-defined center-to-center distance. In this work, 1400, 2100, 2800 and 3500 μm c-t-c distances, are taken into account. All of them are multiple of the minibeam width (700 μm).

In figure 4.10 is an example of depth dose distribution from an array of minibeams. The energy is 195 $MeV/nucleon$ and the c-t-c distance is 1400 μm. In this case, 15 minibeams are overlapping to form the array.
Initially the minibeams are well separated, it means that the dose is distributed for the most along the beams path. In deep, the dose distribution starts to be significant also in the region between two adjacent beams, due to the angular spreading of the beams. At the Bragg peak the dose deposition, for a 1400 μm c-t-c distance, is almost homogeneous.
In figure 4.11, are shown the lateral dose profile at the entrance and at the Bragg peak. At the entrance, the lateral dose profile shows the dose deposited by every beam, as well defined and spaced. At the Bragg peak instead, the lateral dose

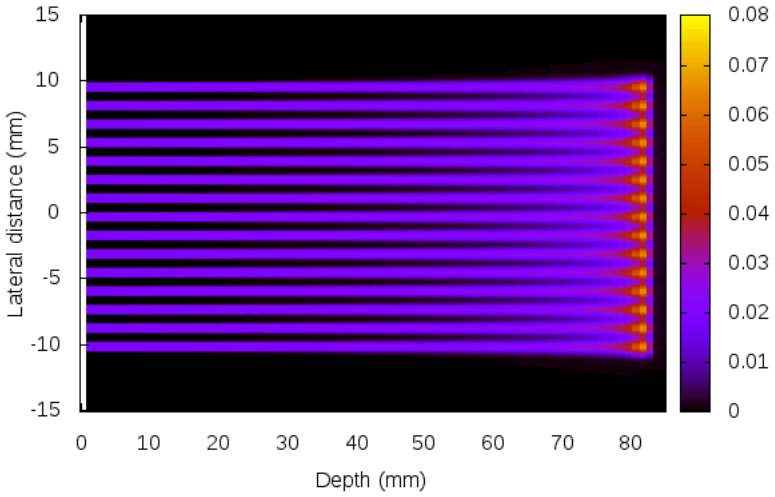

Figure 4.10: *Normalized depth dose deposition for minibeams array with energy 195 MeV/nucleon and 1400 μm c-t-c distance.*

deposition of each beam overlaps with the dose distribution of the beam next to him. Clearly, the dose in the valley region is greater at the Bragg peak than at the entrance, due to the beams superposition. Indeed, the valley dose at the entrance is negligible but in the Bragg peak region this value goes up to the 50% of the dose in the peak region.

The valley dose value depends, between others factors, on the depth and on the c-t-c distance. This raising of the valley dose, reflects a decrement in the PVDR. In figure 4.12, is reported the PVDR as a function of the depth for an array of Carbon minibeams 195 $MeV/nucleon$ and for the SOBP beam for different c-t-c distances. The PVDR decrease rapidly after the entrance, as the valley dose start to increase. In correspondence to the Bragg peak, the PVDR value grows; this is due to the major increase on the dose deposition along the peak region.

In tables 4.4 and 4.5, are shown the PVDR values calculated at different depths for a monochromatic beam (195 $MeV/nucleon$) and for the SOBP beam, as the c-t-c distance changes. The PVDR trend in depth is similar for monochromatic and SOBP beams. The only difference is visible at the Bragg peak, where a bigger increase on the PVDR is obtained for monochromatic beams.

The aim of the radiation therapy is to spare normal tissues giving a solid amount of dose at the target; this goal is reached with the minibeams irradiation technique, when the PVDR values are bigger at the entrance and close to the unit at the Bragg peak. To respect this principle, the best compromises, between the c-t-c distances studied on this work, are 1400 and 2100 μm. For the two c-t-c distances mentioned

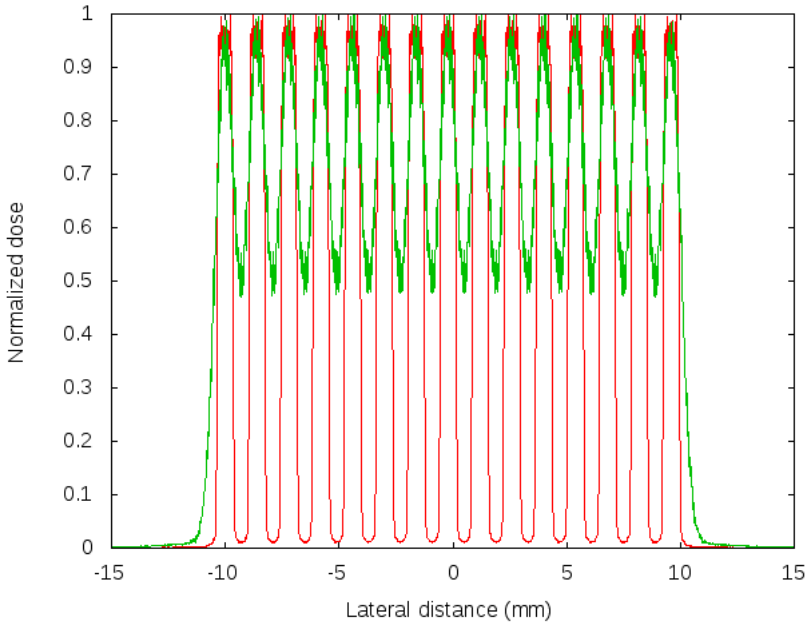

Figure 4.11: *Lateral dose profiles for an array of Carbon minibeams 195 MeV/nucleon and 1400 μm c-t-c distance, calculated at the entrance (in red) and at the Bragg peak (in green).*

above, the PVDR value is less than 10 at the Bragg peak and it is above 10 till 5.5 and 8 *cm* depth for 1400 and 2100 μm c-t-c distance respectively.

In particular, in the case of 1400 μm c-t-c distance, the dose at the target is quasi-homogeneous with a PVDR of 1.8. But the PVDR decrease too rapidly from 79 at 1 *cm* depth to 3.4 at 7 *cm* depth, so PVDR values are not so high in normal tissue. Conversely, for 2100 μm c-t-c distance, the PVDRs are higher in normal tissues, starting from 224 at 1 *cm* depth to 29 at 7 *cm* depth. But in this case, the PVDR is quite high at the Bragg peak too. Indeed a PVDR value of 8 is not enough to ensure a quasi-homogeneous dose at the target.

In order to obtain a quasi-homogeneous dose at the target, an interlaced geometry can be implemented as explained in the next section.

4.6 Minibeams interlaced arrays

A way to spare normal tissue and increase the dose at the target is to implement an interlaced irradiation. The interlaced irradiation is obtained by sending two arrays from opposite directions. The two arrays should be out of phase of half c-t-c distance. In figure 4.13 are shown the depth dose depositions for two interlaced arrays and different c-t-c distances, for a monochromatic minibeam 195 $MeV/nucleon$. The two arrays interlace at the Bragg peak so the valleys of one array are filled with the peaks from the opposite one. It means that a quasi-homogeneous dose distribution

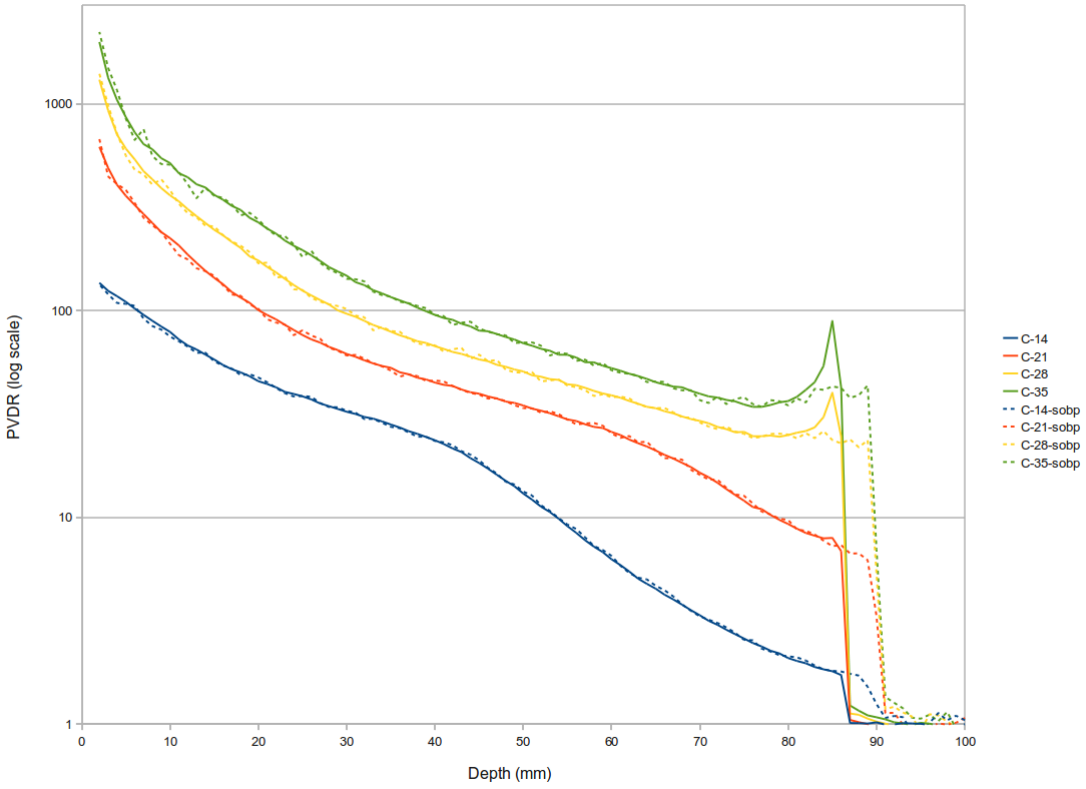

Figure 4.12: *PVDR as function of depth for an array of Carbon minibeams 195 MeV/nucleon and for the SOBP beam for different c-t-c distances.*

at the Bragg peak can be observed.

Looking at the lateral dose profiles (Fig. 4.14) obtained at the Bragg peak for different c-t-c distances, in the interlaced geometry, a quasi-homogeneous dose is obtained for the 1400 μm c-t-c distance. Increasing the c-t-c distance, the dose appears as a follow of peaks and valleys again. The minimum of the dose at the Bragg peak decrease from the 88 % (in the case of 1400 μm c-t-c) to the 23 % (in the case of 3500 μm c-t-c) respect to the maximum dose, as shown in table 4.6.

Using an interlaced geometry, the 2100 μm c-t-c distance, seems to be the best compromise between the c-t-c distances considered, with high values of the PVDR in normal tissues and a quasi homogeneous dose at the target.

PVDR: 195 $MeV/nucleon$ energy beam				
Depth	1400 μm c-t-c	2100 μm c-t-c	2800 μm c-t-c	3500 μm c-t-c
1 cm	79 ± 4	224 ± 11	362 ± 18	518 ± 26
3 cm	32 ± 2	62 ± 3	97 ± 5	148 ± 7
5 cm	13.1 ± 0.7	35 ± 2	51 ± 3	70 ± 3
7 cm	3.4 ± 0.2	16.5 ± 0.8	29 ± 1	40 ± 2
Bragg Peak	1.80 ± 0.09	8.0 ± 0.4	40 ± 2	89 ± 4

Table 4.4: PVDR values for 195 $MeV/nucleon$ carbon minibeam.

PVDR: SOBP beam				
Depth	1400 μm c-t-c	2100 μm c-t-c	2800 μm c-t-c	3500 μm c-t-c
1 cm	75 ± 4	211 ± 11	383 ± 19	509 ± 25
3 cm	33 ± 2	61 ± 3	102 ± 5	144 ± 7
5 cm	13.4 ± 0.7	34 ± 2	50 ± 3	70 ± 43
7 cm	3.3 ± 0.2	16.1 ± 0.8	29 ± 1	37 ± 2
Bragg peak	2.0-1.5 ± 0.1	8.6-6.2 ± 0.4	26-24 ± 1	36-44 ± 2

Table 4.5: PVDR values for SOBP.

Interlaced geometry - dose distribution at Bragg peak	
	percentage minimum dose
1400 μm	88%
2100 μm	76%
2800 μm	48%
3500 μm	23%

Table 4.6: Percentage minimum dose (referred to the maximum) at the Bragg peak for two interlacing arrays at different c-t-c distances.

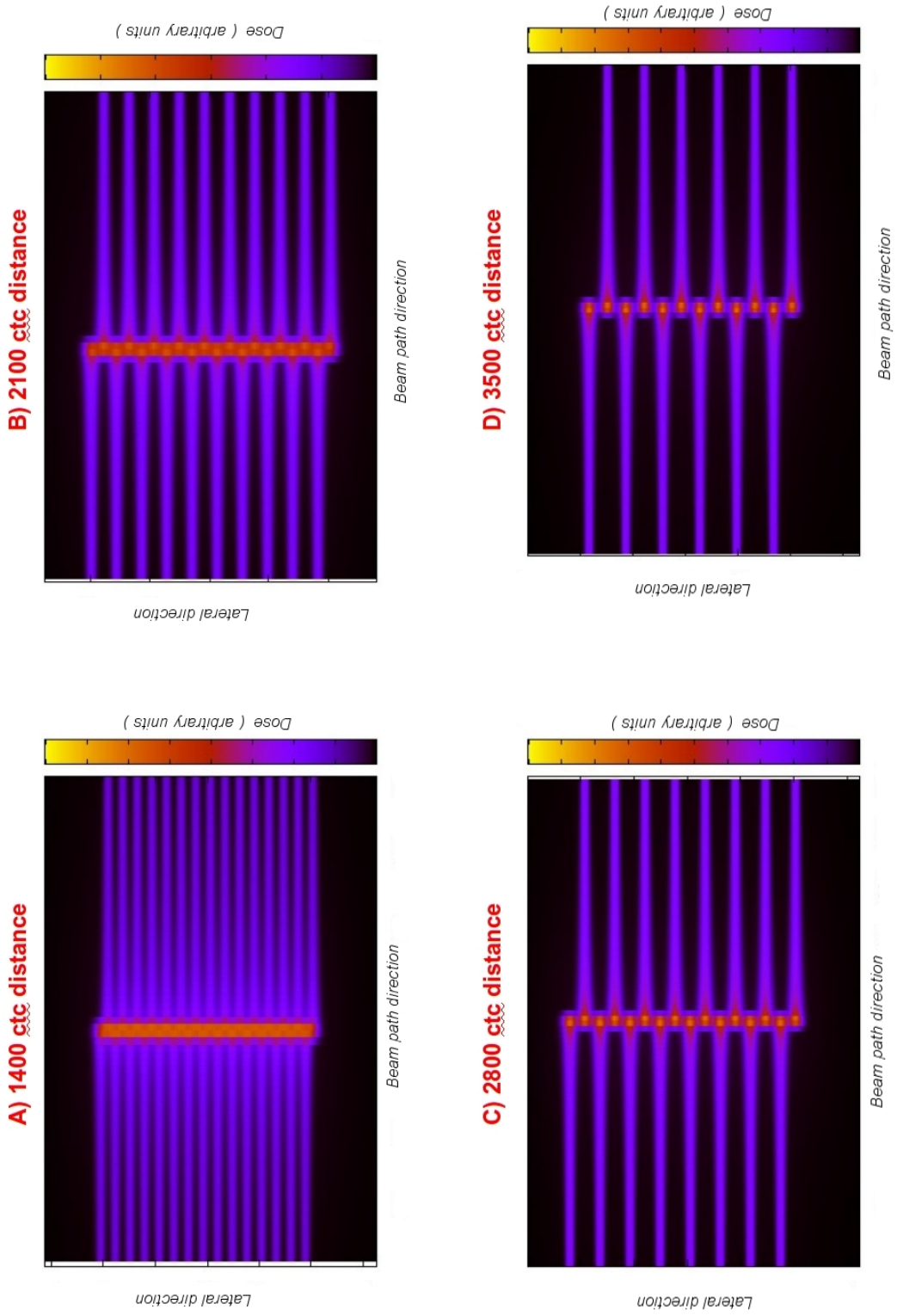

Figure 4.13: *3-D representation of the depth dose distribution for an interlaced geometry for different c-t-c distances.*

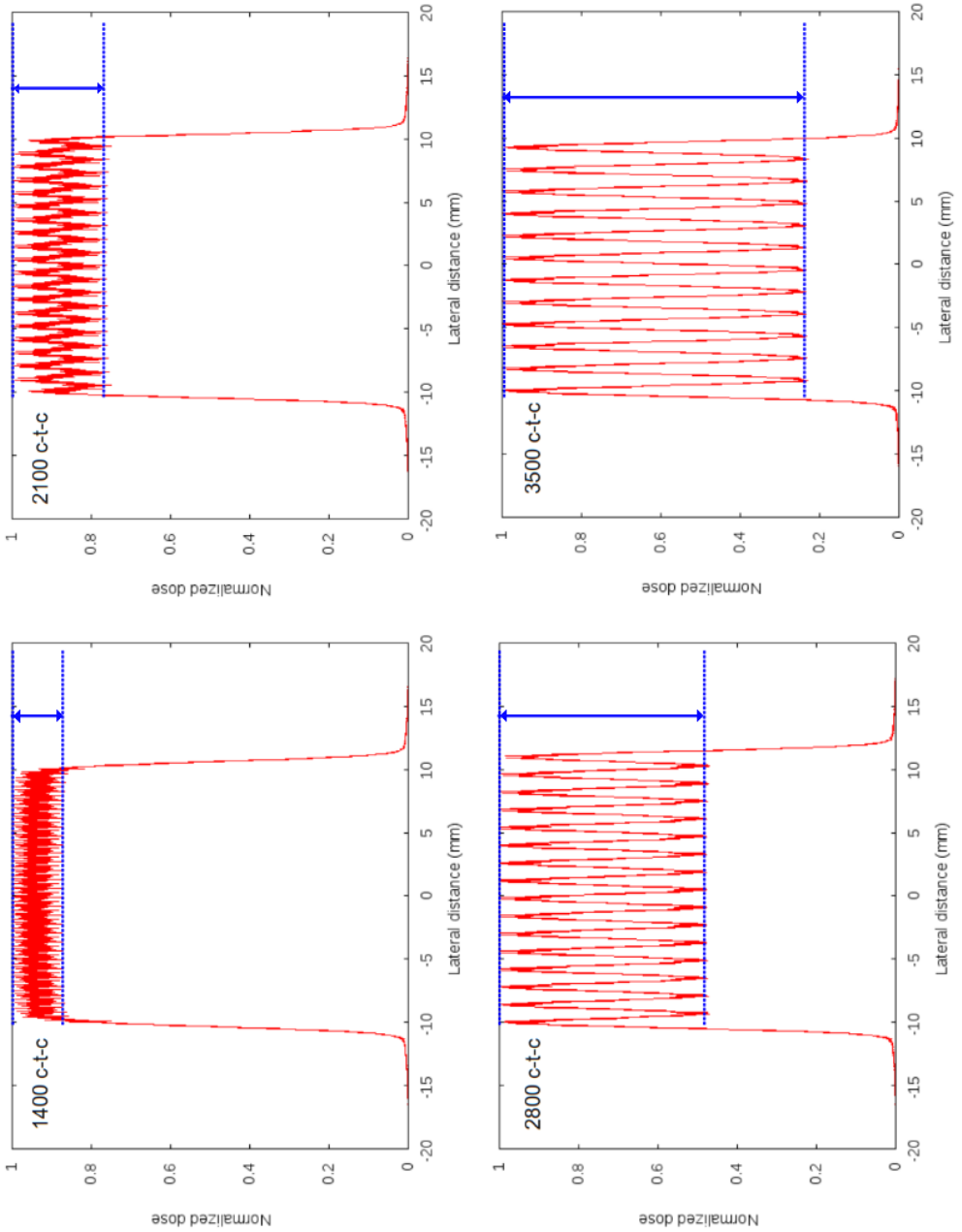

Figure 4.14: *Lateral dose profile at the Bragg peak, for two interlacing arrays at different c-t-c distances.*

Chapter 5

Oxygen minibeams: simulations and results

Contents

In this Chapter, the lateral and depth dose profiles relating to an oxygen minibeams array will be discussed.

As previously done for carbon calculations, a planar minibeam 700 μm wide and 2 cm high impinging on a water cylindrical phantom (as shown in figure 4.1) was used.

The simulations were carried out for different beam energies ranging from 233 to 241 $MeV/nucleon$.

As for the carbon calculations, arrays have been obtained starting from a single beam, through an overlap algorithm. Moreover, summing the Bragg peaks for different energies, the spread out Bragg peak has been obtained. The PVDR were calculated for different array configurations at different c-t-c distances.

5.1 Depth dose profiles for different energies

In order to reach the same depth as done with carbon, an oxygen beam 233.5 $MeV/necleon$ as been used. In figure 5.1, the depth dose distribution for such a beam is shown. The Bragg peak is located at 8 cm depth. The dose deposited at 2 cm depth is about 23% of the dose deposited at Bragg peak.

As done before for the case of carbon minibeams, is necessary to achieve a SOBP by superimposing different Bragg peaks at various energies, in order to obtain a distribution of depth dose covering 1 cm in volume and centered at about 8.5 cm depth. To do so, minibeams of energy between 233.5 and 241.5 $MeV/nucleon$ were simulated; their sum is shown in figure 5.2

The dose rate at 1 cm depth is about 39% of the dose at the SOBP, and the 50% of the dose is obtained from about 6 cm depth.

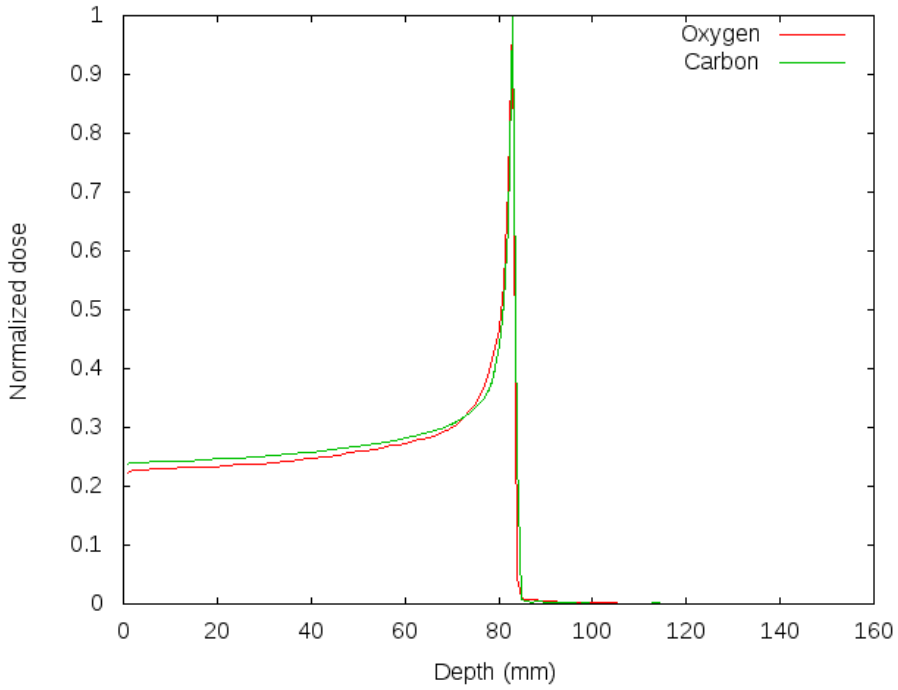

Figure 5.1: *Depth dose distribution for a 233.5 MeV/nucleon oxygen beam (in red).*

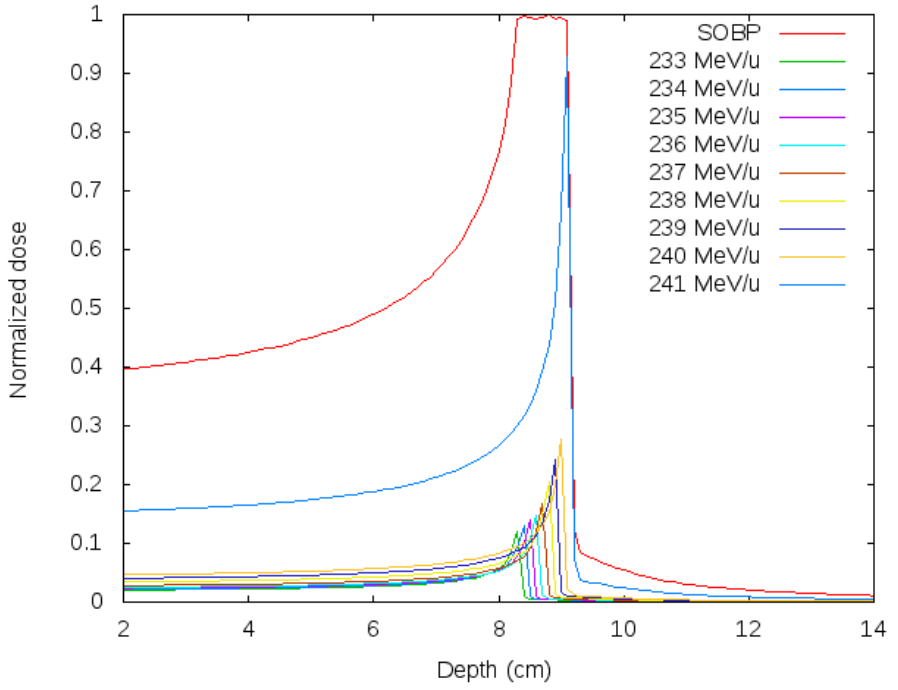

Figure 5.2: *SOBP obtained by a weighted sum of the Bragg peaks from different energies in the range between 233.5 and 241.5 MeV/nucleon.*

Energy (MeV)	Weight
233	0.13
243	0.13
235	0.14
236	0.15
237	0.16
238	0.18
239	0.22
240	0.3
241	1

Table 5.1: Weights used for the composition of the SOBP.

The most significant energy in the SOBP composition is the highest one, as shown in table 5.1, were the relatives weight of each monochromatic beam are reported.

The difference between the dose distributions relating to carbon ions and oxygen ions, is given by the dose tail after the Bragg peak. This tail is due to nuclear fragmentation of the beam and the dose deposited by the fragmentation products. Furthermore, in order to reach the same depth, the oxygen ions must have an energy greater than the carbon ions. This increase in energy affects the amount of dose deposited after the Bragg peak. In the case of oxygen, which is an heavier ion than carbon, this tail appears to be greater than a 2%.

5.2 Lateral dose profiles

The extent of lateral dose deposition depends on the angular scattering of the particles. The lateral scattering increases changing the lateral profile of the beam, as the depth increases.

In figure 5.3, the dose profiles for an oxygen-minibeam with $233 MeV/nucleon$ energy at different depths, are shown. At 1 cm depth, the initial shape of the minibeam appears as a plateau with sharp boundaries. Increasing the depth, the lateral dose profile turns into a Gaussian distribution. As in the case of the figure, for a monochromatic beam 233 $MeV/nucleon$ energy, the Bragg peak is obtained at 8 cm depth, where the major dose deposition is achieved, and the FWHM of the curve is 0.44 mm.

The lateral dose profile, for a SOBP beam, is due to the superposition of the lateral profile for different energies. In figure 5.4, are shown the lateral dose profiles obtained at the same depth (8.0 cm) for different energies, taking into account the weight value in table 5.1 for the composition of the SOBP. Clearly, the most significant energy is the one at 241.5 $MeV/nucleon$.

Comparing the lateral dose profile for a monochromatic beam 233.5 $MeV/nucleon$ and for the SOBP beam (Fig. 5.5), the only difference is on the tails of the distri-

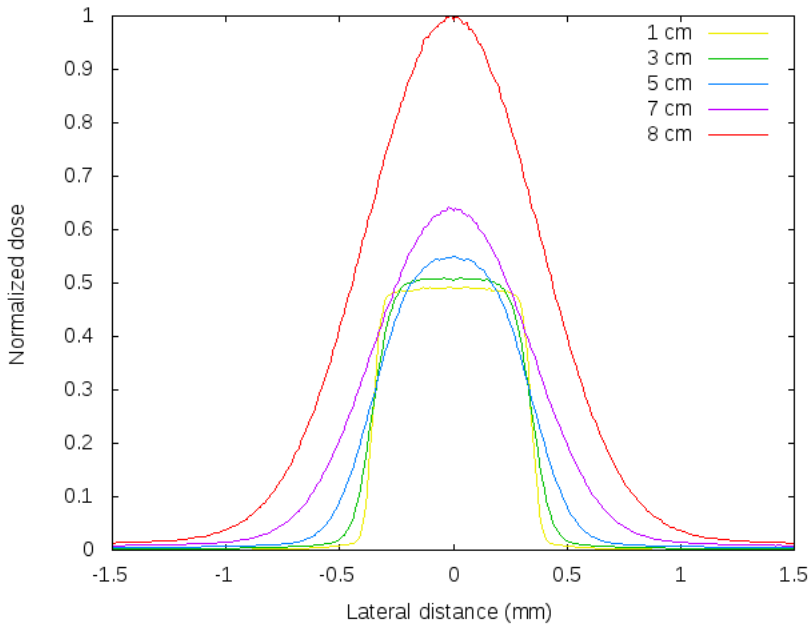

Figure 5.3: *Lateral beam profiles at different depth for an oxygen beam* 233 *MeV/nucleon energy.*

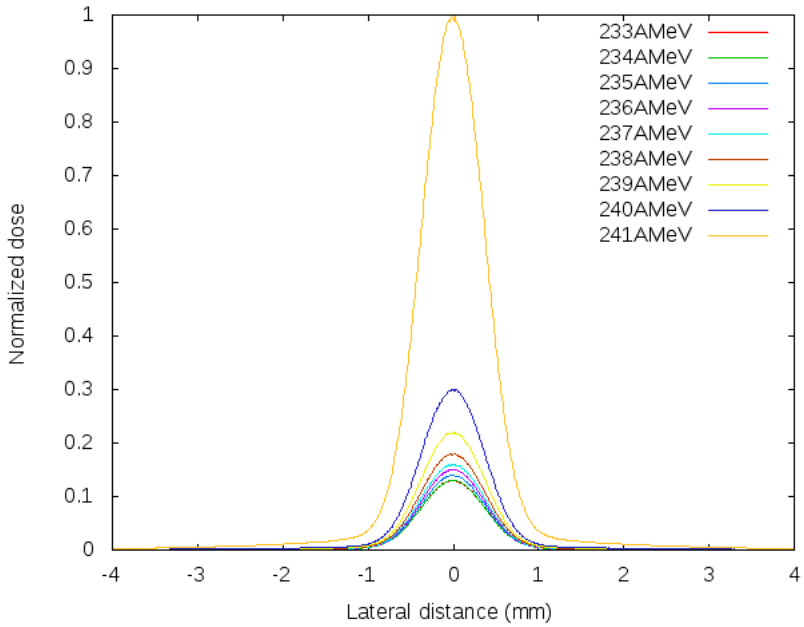

Figure 5.4: *Contributions to the lateral dose profile, due to beams with various energies, at 8.0 cm depth.*

bution. For a SOBP beam, those tails are higher and this influences the valley dose.

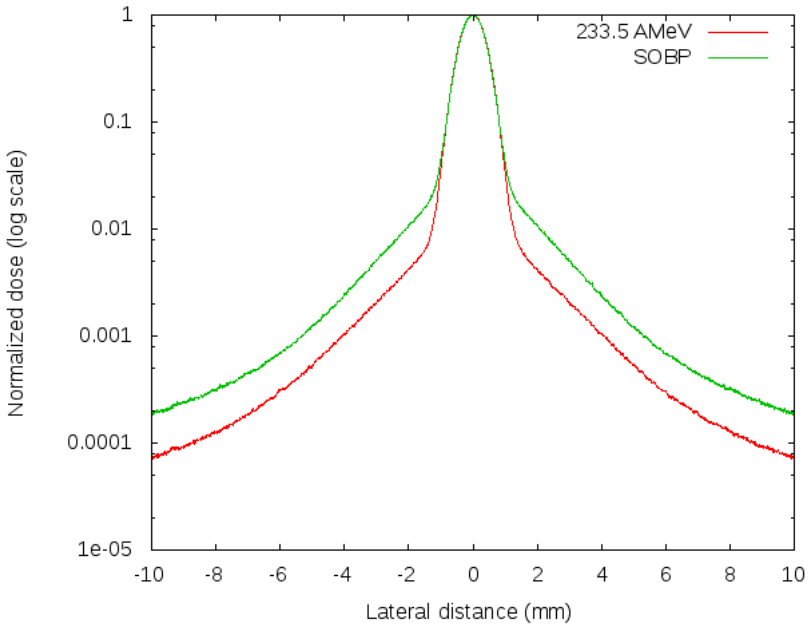

Figure 5.5: *Comparison between the lateral dose deposition for a monochromatic beam 233.5 MeV/nucleon and for the SOBP beam at 8.0 cm depth.*

A study of the penumbra was made, showing the same trend as the previously one for carbon ions. The penumbra values in depth are depicted in figure 5.6.

5.3 Minibeams array and Peak to Valley Dose Ratios

As for Carbon's beam, a code was implemented to calculate the superimpositions of the beams to create an array. The trend of the PVDR in depth can be described by a decreasing curve as shown in figure 5.7, where the PVDR in depth is depicted for an oxygen beam energy 233 $MeV/nucleon$.

The biggest PVDR is obtainend at the entrance, after that it starts to decrease. At about the half depth, it is still 100. It reaches his minimum just before the Bragg peak. At the Bragg peak, there is a slight raise. This increase on the PVDR, it is due to the significant increment on the peak dose. Also the valley dose has an increment at the Bragg peak, but it is not so sharp as for the peak dose. In figure 5.8, a comparison between dose deposition in along the peak region and along the valley region, is shown.

In order for the therapy to be effective, the valley dose should always be below the threshold dose for the considered tissue. And the valley dose is strongly dependent on the center-to-center distance.

As in the previous case of Carbon's beam, the c-t-c distances 1400 μm, 2100 μm,

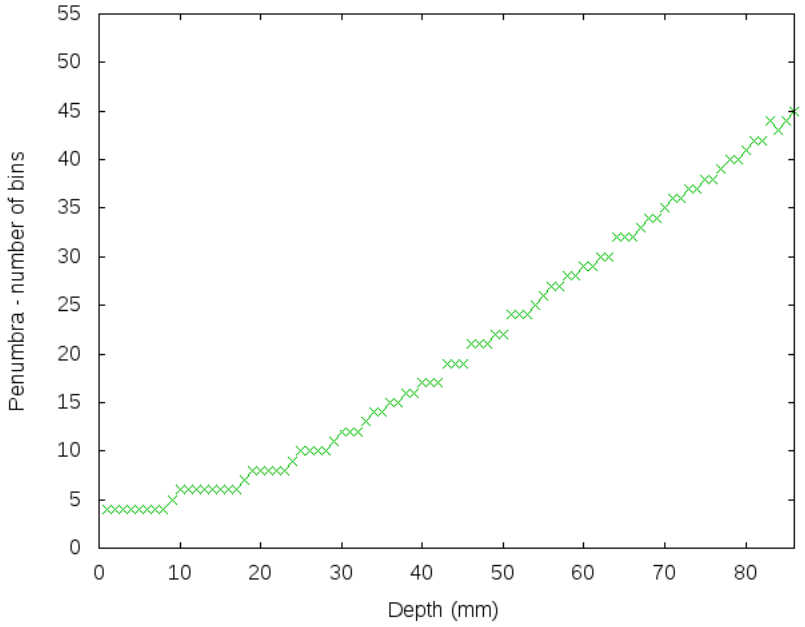

Figure 5.6: *Penumbra values in depth for a monochromatic oxygen beam (237.5 MeV/nucleon).*

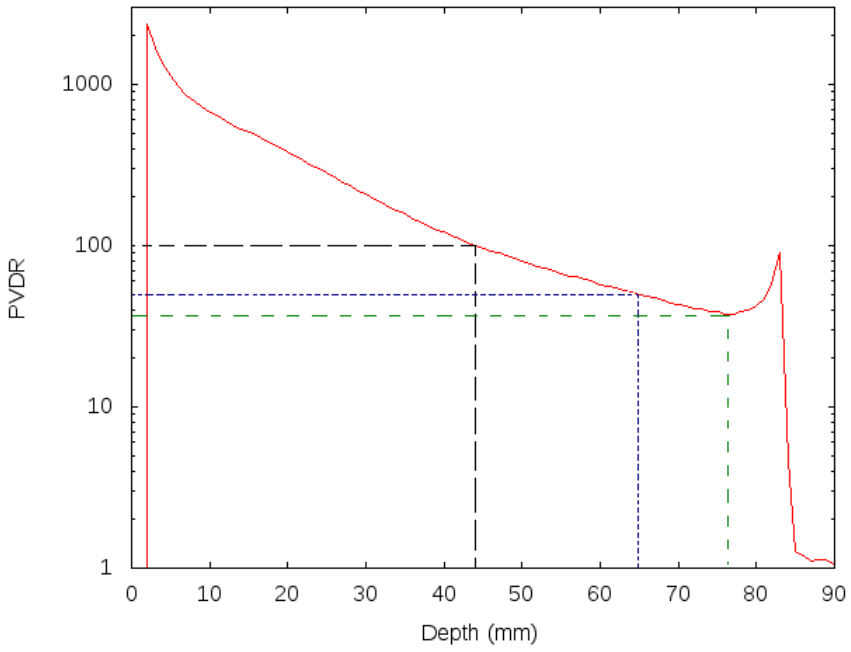

Figure 5.7: *PVDR trend as function of depth in water, for an oxygen beam 233 NeV/nucleon energy.*

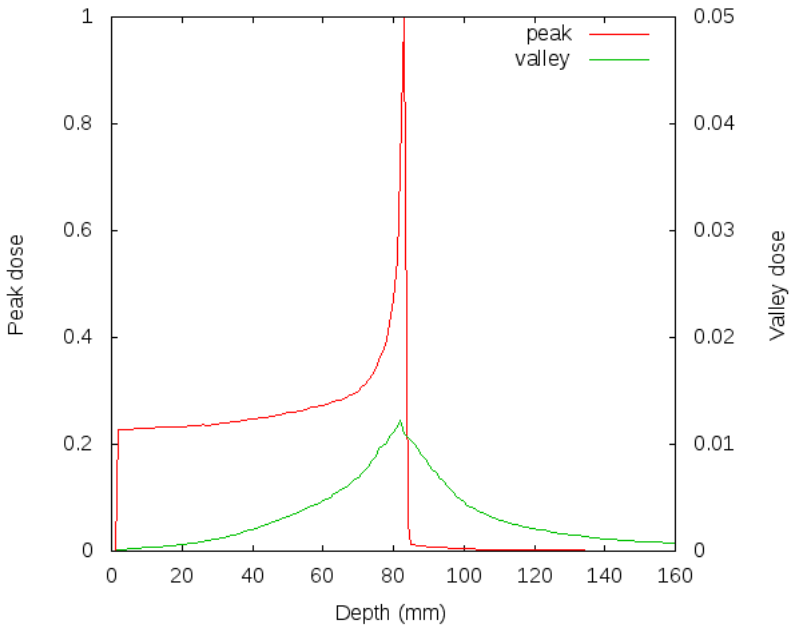

Figure 5.8: *Peak and valley dose deposition are shown separately. The dose deposited in the peak region is shown in red and the scale is at the left side of the plot. For the dose deposited along the valley region (in green), the scale is reported at the right side of the plot.*

2800 μm, 3500 μm were considered. In figure 5.9 are shown two plots: at left is the dose deposition in depth in the valley region, and at right is the PVDR in depth, for different c-t-c distances. A greater valley dose deposition at the Bragg peak for the 1400 μm c-t-c distance configuration, reflects on a PVDR in depth without increment at the Bragg peak. Widening the c-t-c distance, the dose deposited in valley region become lower, and this induces the presence of an increment in the PVDR at the Bragg peak.

For every c-t-c distance, the PVDR was calculated, the results are shown in table 5.2 for a monochromatic beam 233.5 $MeV/nucleon$ energy, and in table 5.3 for the SOBP beam.

PVDR: 233.5 $MeV/nucleon$ energy beam				
Depth	1400 μm c-t-c	2100 μm c-t-c	2800 μm c-t-c	3500 μm c-t-c
1 cm	77 ± 4	260 ± 13	490 ± 24	670 ± 33
3 cm	32 ± 2	70 ± 4	125 ± 6	207 ± 10
5 cm	16.2 ± 0.8	35 ± 2	54 ± 3	81 ± 4
7 cm	4.7 ± 0.2	20 ± 1	31 ± 2	43 ± 2
Bragg Peak	2.6 ± 0.1	17.4 ± 0.8	58 ± 3	90 ± 4

Table 5.2: PVDR values for 233 $MeV/nucleon$ oxygen minibeam.

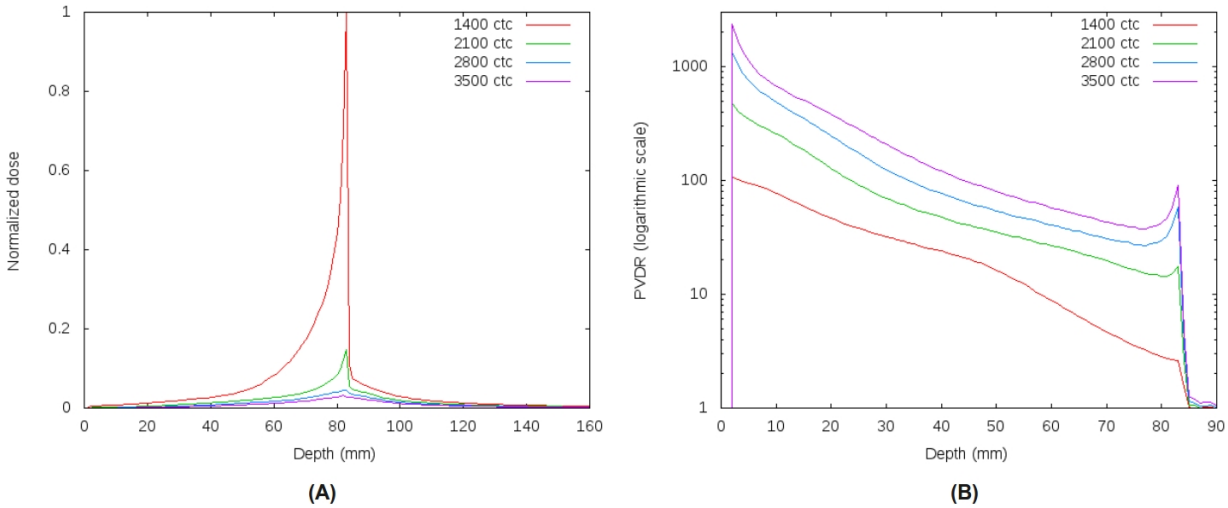

Figure 5.9: *(A) Valley dose in depth for different c-t-c distances. (B) PVDR in depth for different c-t-c distances. These data refer to an oxygen minibeam 233 MeV/nucleon.*

PVDR: SOBP beam				
Depth	1400 μm c-t-c	2100 μm c-t-c	2800 μm c-t-c	3500 μm c-t-c
1 cm	74 ± 4	243 ± 12	470 ± 23	660 ± 33
3 cm	31 ± 2	71 ± 4	129 ± 6	213 ± 11
5 cm	16.5 ± 0.8	35 ± 2	55 ± 3	81 ± 4
7 cm	5.0 ± 0.2	20 ± 1	31 ± 2	44 ± 2
Bragg peak	2.7-2.3	11-12	25-43	35-68

Table 5.3: PVDR values for SOBP.

As previously stated, the PVDR start from a maximum value at the entrance and decreases along the beam path, this is mainly due to the lateral spreading in depth and, consequently, to a rise on the valley dose. For the narrower c-t-c distance (i.e. 1400 μm), the increment in valley dose is quite high, so it is preferable to choose a wider c-t-c distance in order to keep the valley dose in normal tissue as low as possible. The drawback due to the use of c-t-c distances greater than 1400 μm is the increase of the PVDR at Bragg peak. Indeed, a lower PVDR would be appropriate at the Bragg peak so that the dose would be as homogeneous as possible. Anyhow, an homogeneous dose can be reached in the tumor volume, interlacing beams originating from different positions, as explained in next section.

5.4 Minibeams interlaced arrays

Two arrays of minibeams coming from opposite direction interlace at the Bragg peak. This lets to a more homogeneous dose at the Bragg peak.

In figures 5.10 and 5.11, the 3-dimensional depth dose distribution and the lateral profiles at the Bragg peak for the interlaced geometry at different c-t-c distances, are respectively represented.

From the figures, an homogeneous dose deposition at the Bragg peak results for the 1400 μm c-t-c distance. Also, the dose deposited in the interlaced geometry, results to be twice the average dose in the case of a single array.

Increasing the c-t-c distance to 2100 μm, the dose for the interlaced geometry, can be still considered homogeneous because the lower value is still over the 80% of the maximum dose.

For the larger c-t-c distances, 2800 and 3500 μm, the new dose distribution at the Bragg peak due to the interlaced geometry, can be seen as a new array with smaller c-t-c distance. To obtain an homogeneous dose it is necessary to use more arrays of minibeams coming from other directions.

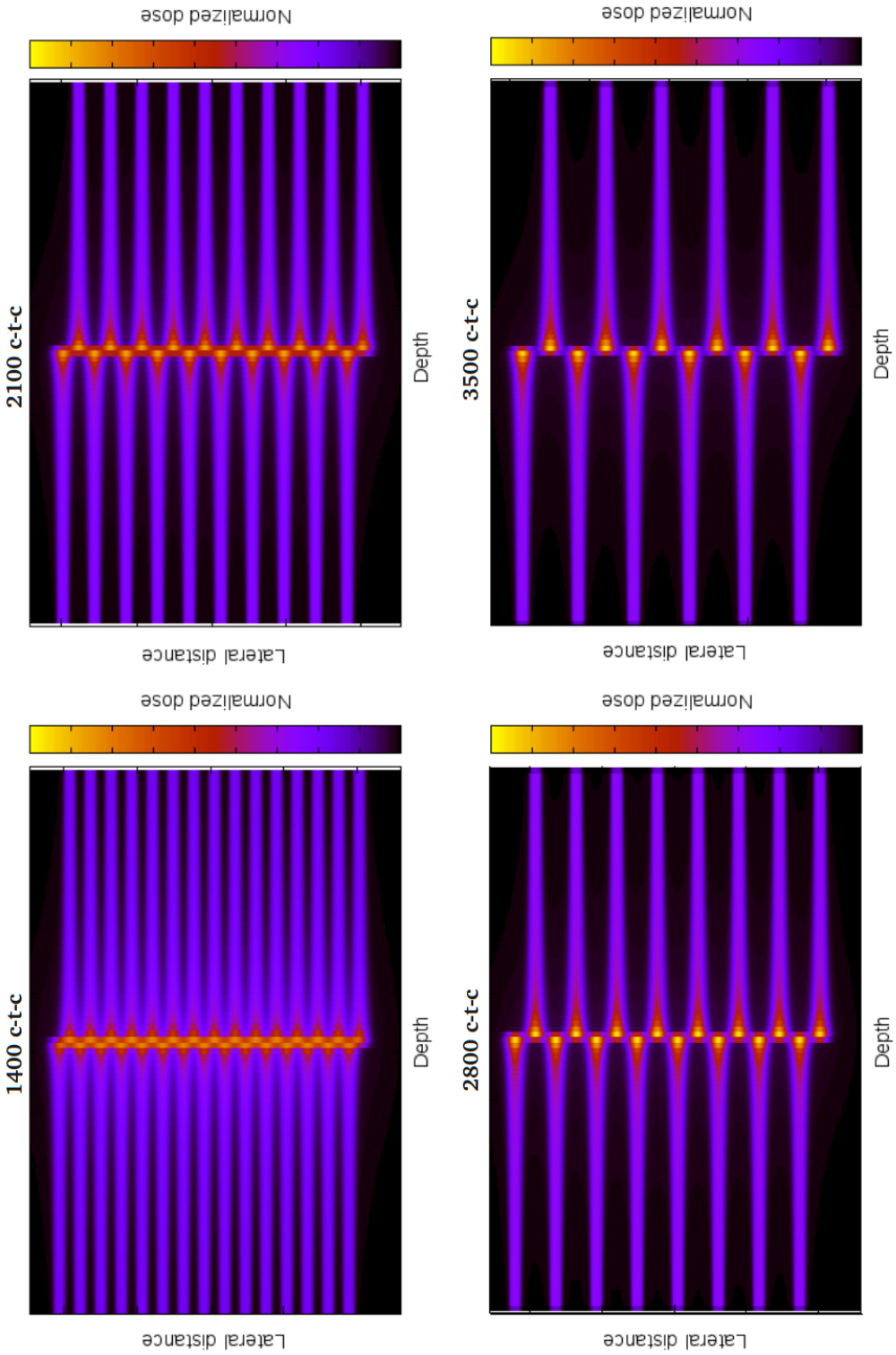

Figure 5.10: *3-D representation of the depth dose distribution for an interlaced geometry for different c-t-c distances.*

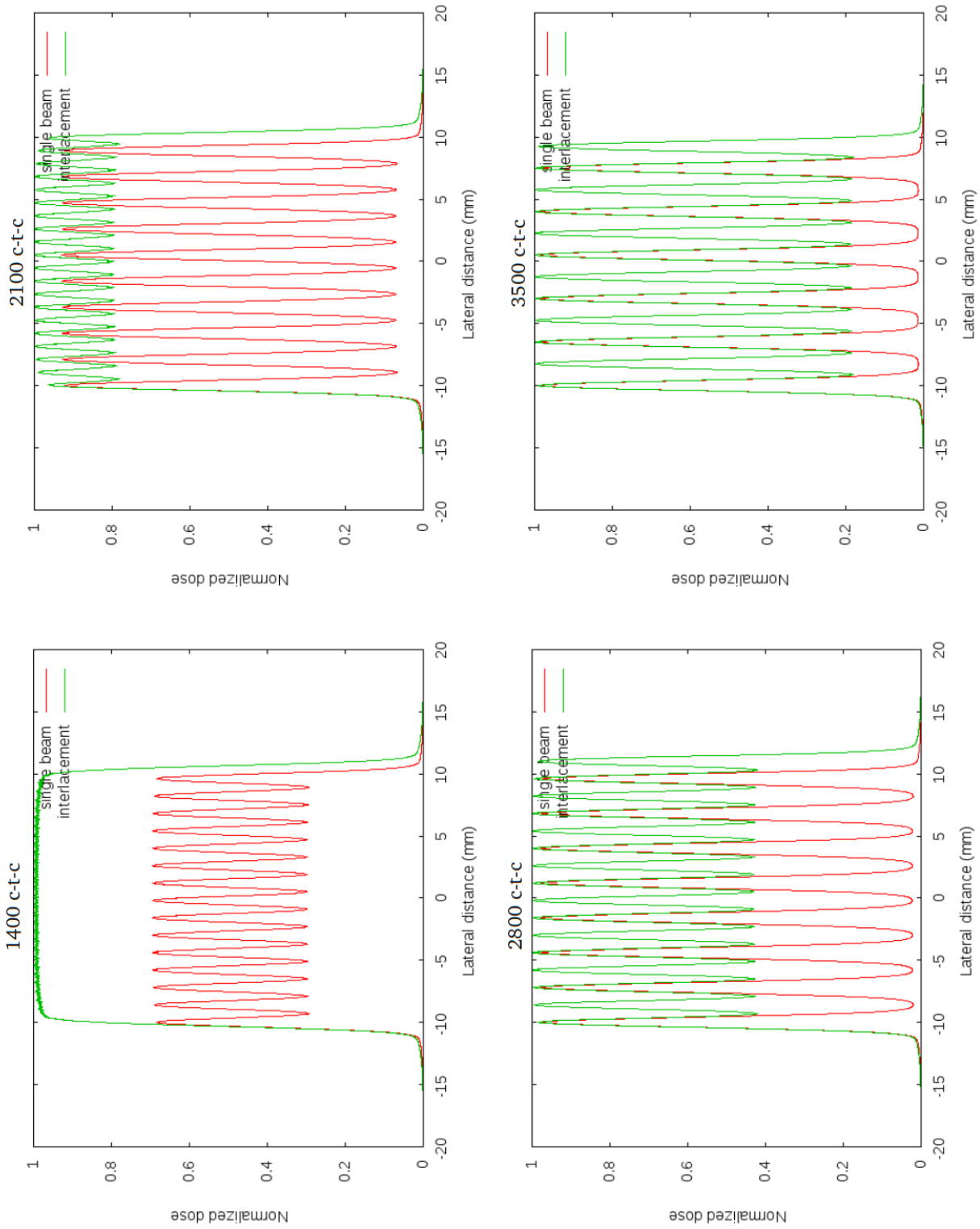

Figure 5.11: *Lateral dose profile at the Bragg peak at different c-t-c distances: for an interlaced geometry (in green), and for a single beam (in red).*

Chapter 6

Results comparisons for Carbon and Oxygen minibeams

Contents

Carbon and oxygen beams in water have been simulated with the aim of evaluating the dose deposition in depth, the lateral dose profiles at different depths, and the ratio of the peak-to-valley doses, being the PVDR a very relevant dosimetric parameter.

Carbon and oxygen present the typical Bragg curve for the dose deposition; in figure 6.1 the depth dose deposition for a carbon beam 200 $MeV/nucleon$ and an oxygen beam 237.5 $MeV/nucleon$ are shown.

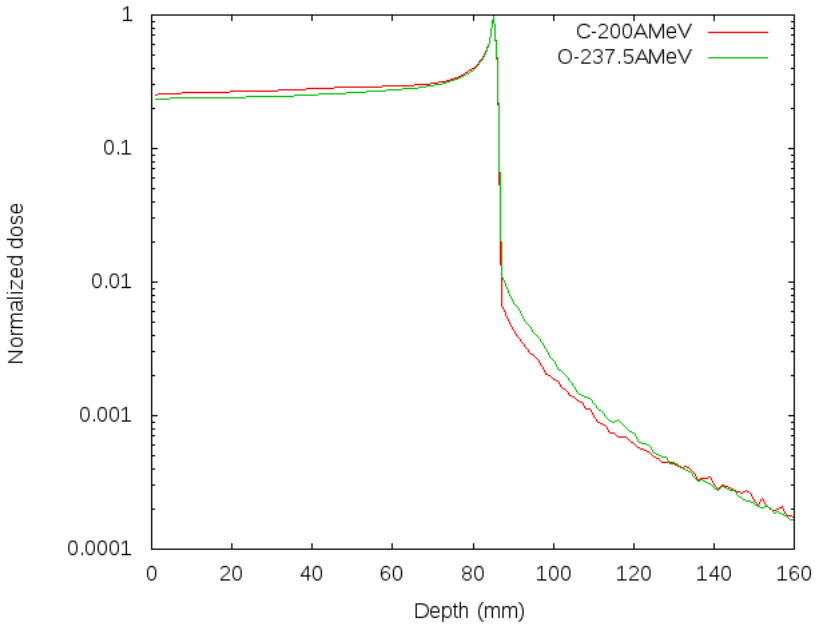

Figure 6.1: *Depth dose deposition in logarithmic scale for a carbon beam 200 MeV/nucleon and an oxygen beam 237.5 MeV/nucleon.*

For those energies, the Bragg peak is obtained at 8.5 cm for both ions. The

main difference for the two beams lies on the dose deposited after the Bragg peak due to the fragmentation processes. This tail beyond the Bragg peak is higher for oxygen ions than for carbon ions.

From the simulations, was also possible to study the lateral spreading of the beams. In figure 6.2 are shown the lateral dose profiles at the Bragg peak for both the ion beams. Carbon beam presents a lateral spreading larger than oxygen, due

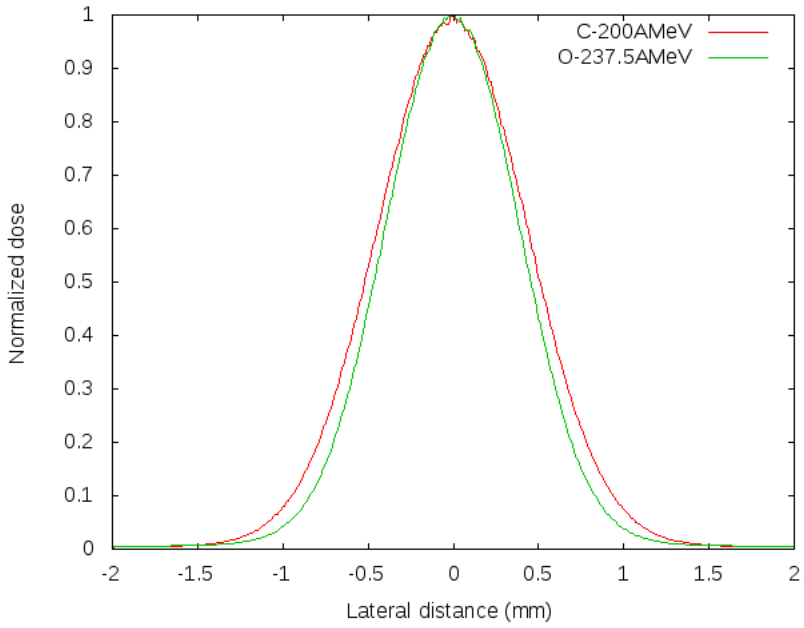

Figure 6.2: *Lateral dose deposition for a carbon beam 200 MeV/nucleon (in red) and an oxygen beam 237.5 MeV/nucleon (in green).*

to a greater angular spreading.
At the same way, the data for the penumbra show bigger values for carbon beam than for oxygen beam. In figure 6.3, the values of the penumbra calculated along the beam path, are shown for carbon and oxygen minibeams.

The study on lateral spreading for the two ions, is the first step towards the study of the most important parameter for the technique: the PVDR.

In figure 6.4 are shown the PVDR in depth at different c-t-c distances for both carbon and oxygen ions.

The PVDR values for oxygen are always greater than for carbon, with the exception of the Bragg peak region for 1400 μm c-t-c distance.

For both ions, the suitable c-t-c distance seems to be 2100 μm. This is the distance with the best compromise between high PVDR at the entrance and low PVDR at the target.

An important factor that will make the difference between the two ions is the

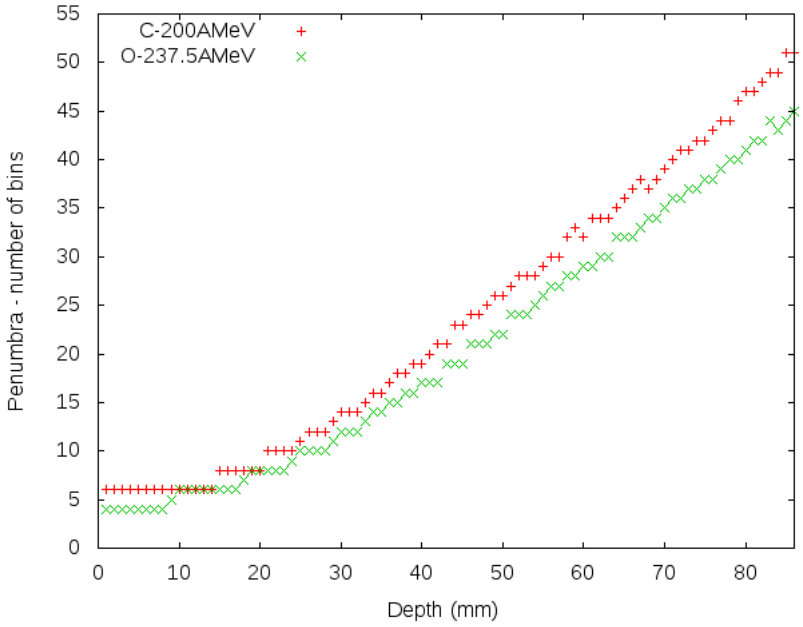

Figure 6.3: *Penumbra values as a function of depth for a carbon beam 200 MeV/nucleon (in red) and an oxygen beam 237.5 MeV/nucleon (in green).*

RBE. Since RBE of charged particles is increased by increasing the particle ionization density, biological effectiveness is close to that of x-rays in the entrance channel where normal tissue is exposed, and is high in the Bragg peak region where the tumor is located.

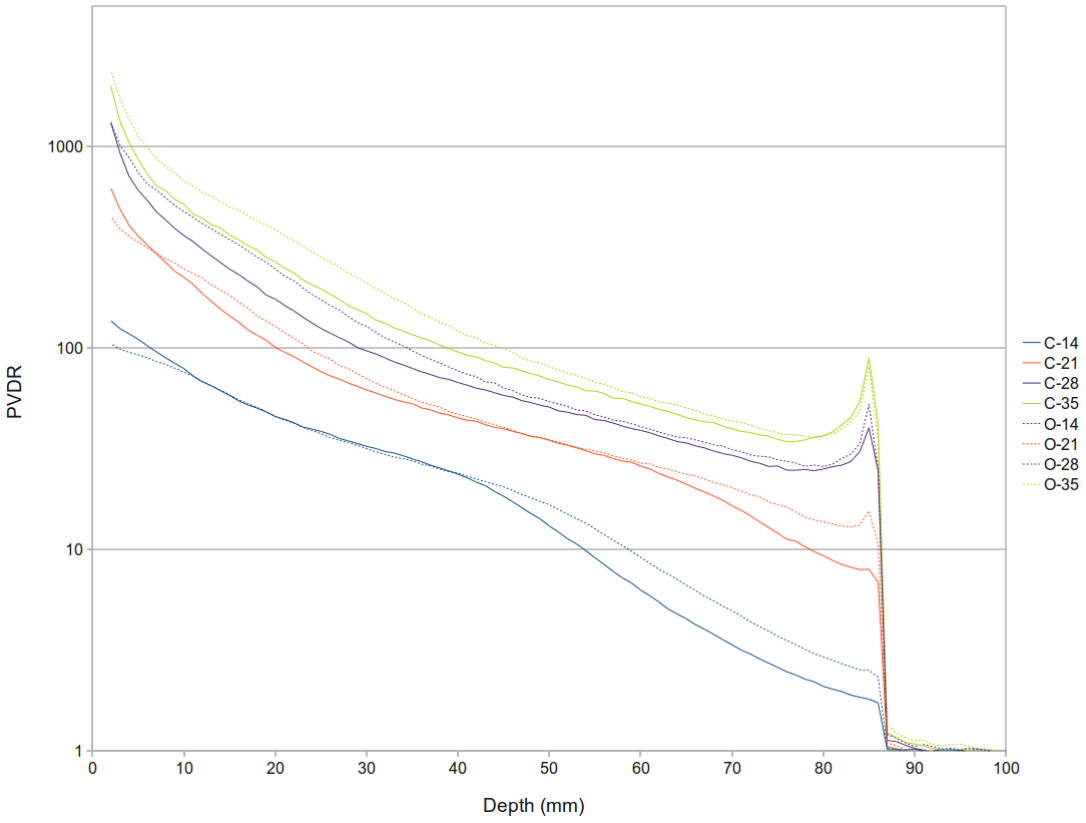

Figure 6.4: *PVDR values as a function of depth for a carbon and oxygen minibeam arrays, at different c-t-c distances.*

6.1 Comparison with x-rays minibeams

In a study on minibeam radiation therapy conducted at the ESRF [29], Monte Carlo simulations were used to calculate penumbra and PVDR in the healthy tissues and in the tumor for different beam energies. On that work, x-rays 600 μm minibeam size and 1200 μm c-t-c separation were considered.

For x-rays with energy between 100 and 500 keV and c-t-c distance of 1200 μm, penumbra values at the target (7 cm depth) were found to be between 20 $\pm$ 1 μm and 230 $\pm$ 11 μm, corresponding to the 3% and 38% of the initial beam width. Those values are much smaller than the values found for carbon and oxygen ions that are between 400-450 μm ($\approx$ 60% of the initial beam width).

The PVDR values have been found to be much smaller for x-rays than for carbon and oxygen. For x-rays, the PVDRs range between 7.8 at the target for 500 keV and 34 at the entrance for 400 keV. The PVDR found with the simulation in this work are much bigger, ranging between 1.8 at the target and 79 at the entrance, for carbons; and ranging between 2.6 at the target and 77 at the entrance, for oxygen (those values are referred to a c-t-c distance of 1400 μm).

Chapter 7

Spatially fractionnated Grid therapy with protons

Contents

Among the recent techniques in the treatment of cancer is the use of a perforated grid in radiation therapy.

Köhler was the first to report on the use of a grid in x-ray therapy in 1909. The literature contains no other reference to this form of treatment until 1933, when Liberson, unaware of the previous report, developed the same idea. He found that the skin could tolerate larger doses and would recover more quickly when the radiation was delivered through a grid [47].

In Grid therapy the radiation is delivered using a grid-like pattern of small beams, and it enables delivery of higher tumor doses while minimizing radiation-induced skin damage.

Grid therapy is based on the dose-volume effect, in which dose delivered to a continuous region induces greater cell damage than the same dose fractionated in space. As for microbeam therapy in which reducing a radiation beam diameter from 1 mm to 25 μm increased the threshold dose for destruction of cells along the beam path, the parts of the tissue that are not irradiated can help repair areas that are irradiated.

Previous studies have used a single photon field to deliver the grid pattern, resulting in the dose distribution of peaks and valleys being applied to both normal tissue and the tumor. Whilst this approach does indeed improve normal tissue sparing, it also reduces the therapeutic effect to the tumor.

The idea is to use protons pencil beams to create grid-like entrance doses, while ensuring homogeneous dose coverage of the target volume.

7.1 Simulation parameters

As for the case of carbon and oxygen minibeams, a cylindrical water geometry was implemented. To collect data, two boxes with dimension 1×1 cm along x and y

directions, and 1 mm in depth (z direction), were used. One of the boxes was placed at the entrance (1 cm deep), and the second one was placed at the Bragg peak.

The source was a square proton minibeam 700 μm per side. For the energy of the beam a Gaussian distribution with 2 MeV σ was implemented. The central energy was 105 MeV.

The dose was collected inside the boxes above, by a doseActor (section 3.2.3). The box was divided in $1000 \times 1000 \times 1$ voxels. So the voxel shape is a cube with dimension of 1 mm per side.

The number of primary showers was 10^7.

7.2 Depth dose curve

In this section the depth dose distribution for proton beams of 105 MeV energy are presented. In figure 7.1 the depth dose curve for one complete array of minibeams is shown. The Bragg peak is obtained at 8.2 cm depth, negligible dose is deposited at depths higher than 9 cm. The data plotted in figure 7.1 were collected in voxels

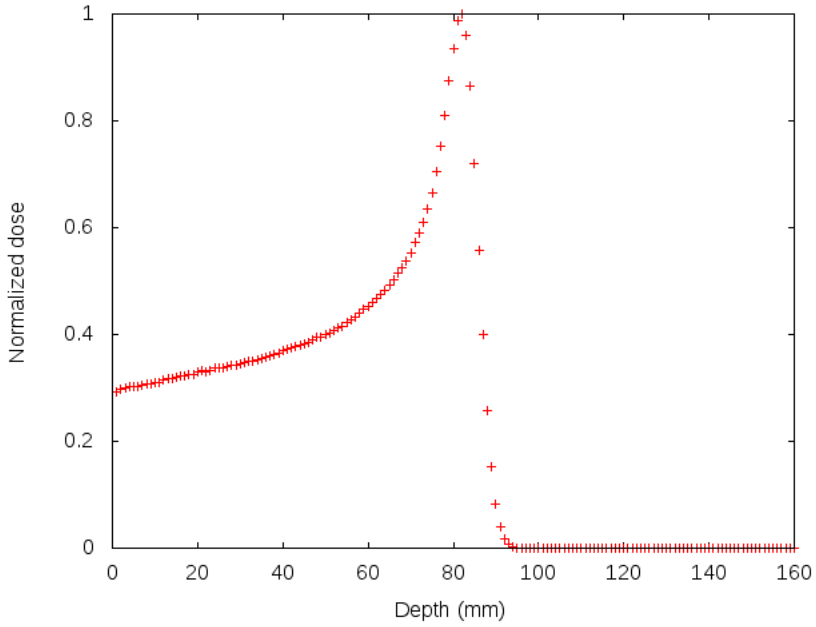

Figure 7.1: *Depth dose curve for an array of proton minibeams 105 MeV energy. Data were sampled with voxels* $2cm \times 2cm \times 1mm$.

of $2cm \times 2cm \times 1mm$ dimension to cover the whole array so both the primary and scatter beams are taken into account.

In figure 7.2 is shown the depth dose profile for a single proton minibeam 105 MeV energy. In this case the voxels size is $700\mu m \times 700\mu m \times 1mm$. The shape differs from the standard depth dose curve for protons due to the high ratio of the lateral scattering with respect to the dose deposited by the primary beam.

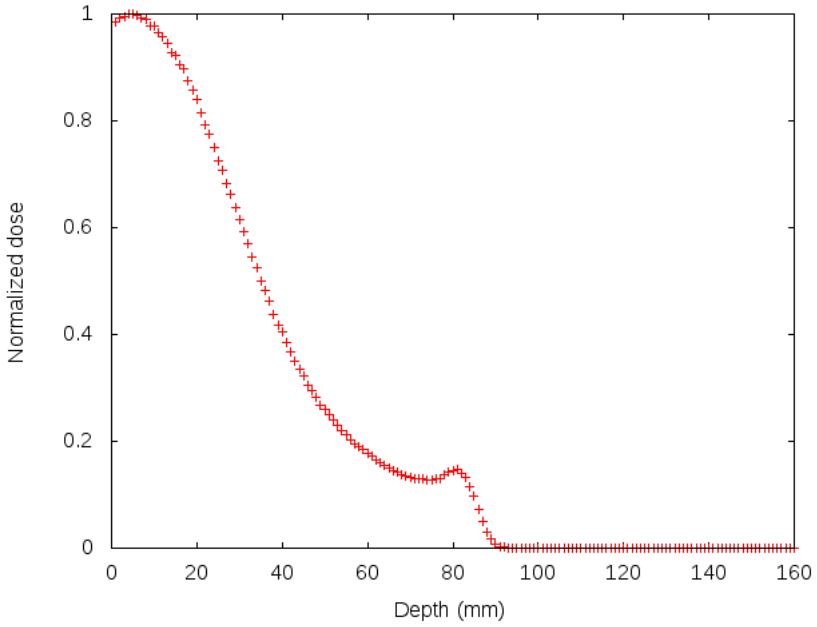

Figure 7.2: *Depth dose curve for an array of proton minibeams 105 MeV energy. Data were sampled with voxels* $700\mu m \times 700\mu m \times 1mm$.

7.3 Grid simulations

A square proton minibeam with dimensions 700 μm per side, energy 105 MeV and impinging on a cylinder of water, was simulated. The arrays of square minibeams was creating through an algorithm. The c-t-c distances 1400, 2100, 2800 and 3500 μm have been considered.

In figure 7.3, are shown the lateral dose deposition for an array with 1400 μm c-t-c distance, at the entrance (1 cm depth) and at the Bragg peak.

At the entrance, the grid geometry is well defined, every single beam composing the array can easily be distinguished. At the Bragg peak, the angular spreading of the beams, leads to a homogeneous dose and the single beams cannot be distinguished anymore.

Increasing the c-t-c distance to 2100 μm, the dose at the Bragg peak is still homogeneous, as shown in figure 7.4. For the other c-t-c distances, 2800 (Fig. 7.5) and 3500 (Fig.7.6) μm, the dose at the Bragg peak is less homogeneous, but the PVDR are still small as shown in table 7.1, where the PVDR for different c-t-c distances are reported.

For this configuration, the 2100 μm c-t-c distance, seems to be the most favorable one, since produce a PVDR of about 1 at the Bragg peak and a much higher value of 300 at the entrance.

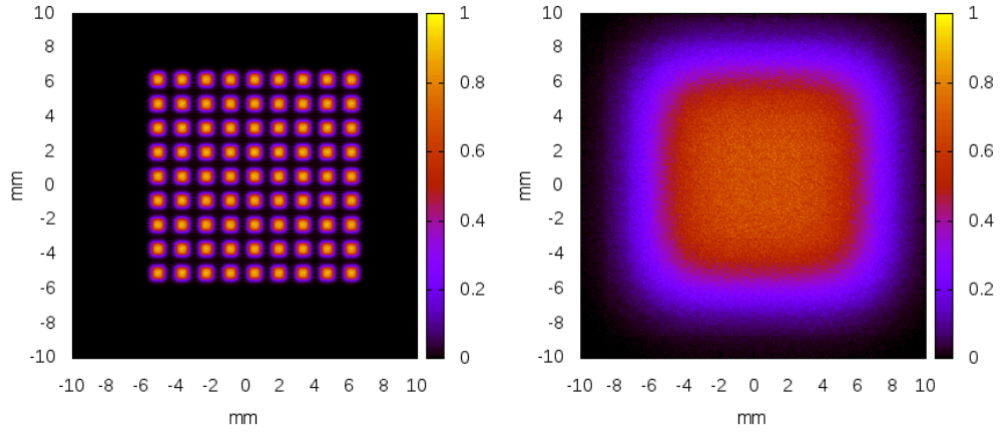

Figure 7.3: *Lateral dose deposition for an array of proton minibeams with 1400 µm c-t-c distance, at the entrance (left) and at Bragg peak (right).*

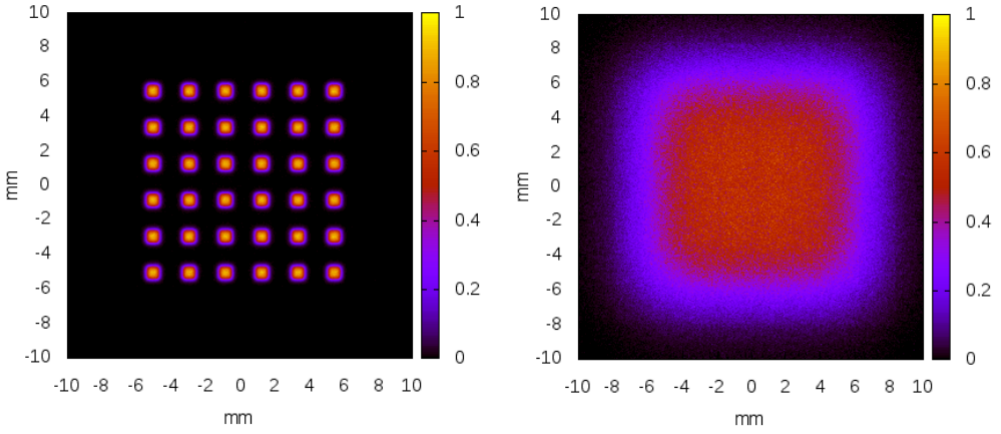

Figure 7.4: *Lateral dose deposition for an array of proton minibeams with 2100 µm c-t-c distance, at the entrance (left) and at Bragg peak (right).*

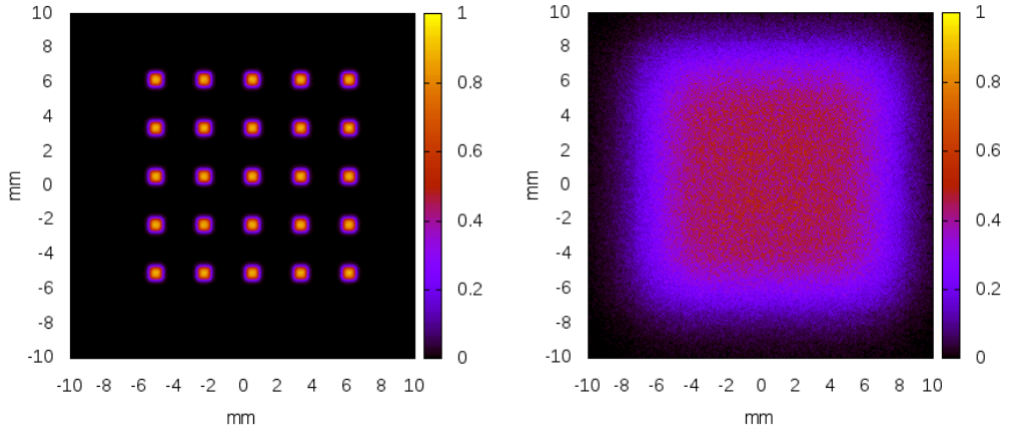

Figure 7.5: *Lateral dose deposition for an array of proton minibeams with 2800 µm c-t-c distance, at the entrance (left) and at Bragg peak (right).*

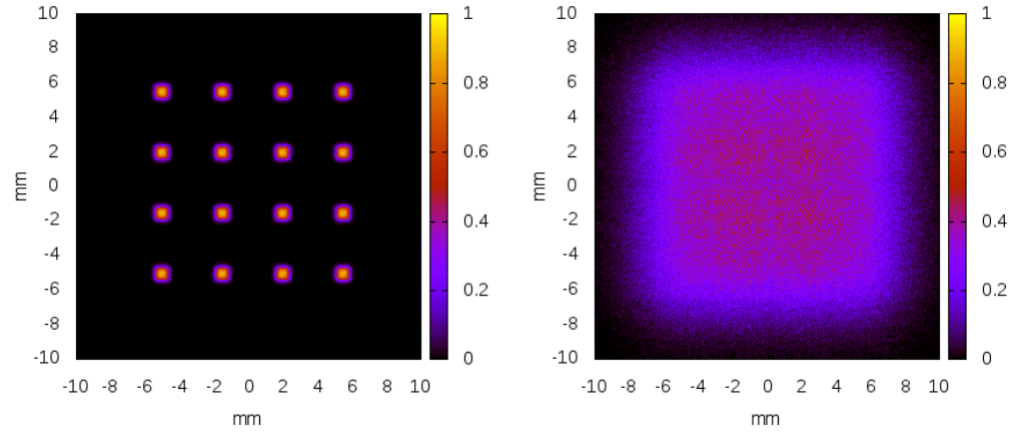

Figure 7.6: *Lateral dose deposition for an array of proton minibeams with 3500 µm c-t-c distance, at the entrance (left) and at Bragg peak (right).*

PVDR values		
c-t-c distance (μm)	Entrance	Bragg peak
1400	60 ± 3	1.0 ± 0.1
2100	310 ± 15	1.0 ± 0.1
2800	850 ± 40	1.5 ± 0.1
3500	3000 ± 150	2.0 ± 0.2

Table 7.1: PVDR values for an array of proton minibeams at different c-t-c distances.

Discussion

Minibeam radiation therapy (MBRT) is a technique that explores the limits of the dose volume effect by the use of submillimetric field sizes in combination with the spatial fractionation of the dose.

MBRT with synchrotron x-ray is presently under development at Brookhaven National Laboratory and at the European Synchrotron Radiation Facility.

This thesis work has been devoted to the study of MBRT with heavy ions instead of x-rays. In particular Carbon and Oxygen beams have been taken into account. The aim was to put together the advantages of spatially fractionated techniques with the advantages of a better ballistic typical of hadrontherapy.

By means of Monte Carlo simulations, the depth dose distributions, the lateral distributions, the Peak-to-Valley-Dose ratios (PVDR) were calculated for carbon and oxygen beams at different energies and different center-to-center distances.

As a result, a slightly larger lateral spreading for carbon, leading to larger values on the penumbra of the beam respect to the oxygen case, was found. A bigger tail deposition beyond the Bragg peak due to fragmentation process, was found for oxygen.

Finally the study of the PVDR as function of the center-to-center distance between the minibeams, point at 2100 μm as the best compromise between giving a quasi-homogeneous dose at the target and sparing normal tissues, for the center-to-center distances taken into account in this study.

From a comparison with x-rays minibeams data, was found that heavy ions produce larger penumbras. On the contrary, PVDRs were found to be more competitive, since higher values were found at the entrance and smaller values were found at the target.

Among the spatially fractionated techniques grid therapy should be included. Even in the case of the grid therapy, the concept has been revised considering the use of protons instead of x-rays. From the simulations was proved the possibility to obtain a homogeneous or quasi-homogeneous dose at the target while retaining high values of PVDR along the beam path, for all the center-to-center distances considered.

In conclusion, this proof of concept has demonstrated that spatially fractionated techniques such as MBRT and grid can also be implemented with the use of ions instead of x-rays, exploiting the advantages of hadrontherapy.

Bibliography

[1] WHO. World cancer report. Technical report, World Health Organization, Geneva, 2008. (Cited on page 1.)

[2] ACS. Cancer facts and figures 2012. Technical report, American Cancer Society, Atlanta, United States of America, 2012. (Cited on page 1.)

[3] IAEA. Planning national radiotherapy services: a practical tool. Technical report, International atomic energy agency, Vienna, 2010. (Cited on page 1.)

[4] E. B. Podgorsak. *Radiation Oncology Physics: A handbook for teachers and students*. IAEA, 2005. (Cited on pages 4, 22, 23, 26, 27 and 28.)

[5] Xing L., Thorndyke B., Schreibmann E., Yang Y., Li T.F., Kim G., Luxton G., and Koong A. Overview of image-guided radiation therapy. *Medical Dosimetry*, 31(2):91–112, 2066. (Cited on page 4.)

[6] AAPM. The menagement of respiratory motion in radiation oncology. Technical report, American Association of Physicists in Medicine, College Park, MD 20740-3846, 2006. (Cited on page 4.)

[7] Yan D., Vicini F., Wong J., and Martinez A. Adaptive radiation therapy. *Phys Med Biol*, (42):123–32, 1997. (Cited on page 4.)

[8] M. K. Buyyounouski, R. A. Price, E. E. R. Harris, R. Miller, W. Tomé, T. Schefter, E. I. Parsai, A. A. Konski, and P. E. Wallner. Stereotactic body radiotherapy for primary management of early-stage, low-to intermediate-risk prostate cancer: report of the american society for therapeutic radiology ancd oncology emerging technology commitee. *Int. J. Radiation Oncology Biol. Phys.*, 76(5):1297–1304, 2010. (Cited on page 5.)

[9] D. N. Slatkin, P. Spanne, F. A. Dilmanian, and M. Sandborg. Microbeam radiation therapy. *Medical Physics*, 19(6), 1992. (Cited on page 5.)

[10] D. N. Slatkin, P. Spanne, F. A. Dilmanian, J. O. Gebbers, and J. A. Laissue. Subacute neuropathological effects of microplanar beams of x-rays from a synchrotron wiggler. *Proc. Natl. Acad. SCi. USA*, 92(19), 1995. (Cited on page 5.)

[11] W. Thomlinson, P. Berkvens, G. Berruyer, B. Bertrand, H. Blattmann, E. Bräuer-Krisch, T. Brochard, A.M. Charvet, S. Corde, M. Dimichiel, H. Ellaume, Esteve F., S. Fiedler, J. A. Laissue, J. E. Le Bas, G. Le Duc, N. Lyubimova, C. Nemoz, M. Renier, D. N. Slatkin, P. Spanne, and P. Suorti. Research at the european synchrotron radiation facility medical beamline. *Cell Mol Biol*, 46(6), 2000. (Cited on page 5.)

[12] E. Bräuer-Krisch, H. Requardt, P. Regnard, S. Corde, E. Siegbahn, G. Le Duc, T. Brochard, H. Blattmann, J. A. Laissue, and A. Bravin. New irradiation geometry for microbeam radiation therapy. *Phys Med Biol*, 50(13), 2005. (Cited on page 5.)

[13] F. A. Dilmanian, Y. Qu, S. Liu, C.D. Cool, J. Gilbert, J.F. Hainfeld, C.A. Kruse, J. Laterra, D. Lenihan, M. M. Nawrocky, G. Pappas, C.I. Sze, T. Yuasa, N. Zhong, Z. Zhong, and J. W. McDonald. X-ray microbeams: tumor therapy and central nervous system research. *Nucl. Instrum. Methods Phys. Res. A*, 548(1-2), 2005. (Cited on page 5.)

[14] F. A. Dilmanian, G. M. Morris, G. Le Duc, X. Huang, B. Ren, T. Bacarian, J. C. Allen, J. Kalef-Ezra, I. Orion, E. M. Rosen, T. Sandhu, T. Sathe, X. Y. Wul, Z. Zhong, and H. L. Shivaprasad. Response of avian embryonic brain to spatially segmented x-ray microbeams. *Cell. Mol. Biol.*, 47:485–493, 2001. (Cited on pages 5 and 6.)

[15] F. A. Dilmanian, T. M. Button, G. Le Duc, N. Zhong, L. A. Peña, J. A. L. Smith, S. R. Martinez, T. Bacarian, J. Tammam, B. Ren, P. M. Farmer, J. Kalef-Ezra, P. L. Micca, M. M. Nawrocky, J. A. Niederer, F. P. Recksiek, A. Fuchs, and E. M. Rosen. Response of rat intracranial 9l gliosarcoma to microbeam radiation therapy. *Neuro Oncol.*, 4:26–38, 2002. (Cited on pages 5 and 6.)

[16] F. A. Dilmanian, Y. Qu, L. E. Feinendegen, L. A. Peña, T. Bacarian, NewAuthor6, F. A. Henn, J. Kalef-Ezra, S. Liu, Z. Zhong, and J. W. McDonald. Tissue-sparing effect of x-ray microplanar beams particularly in the cns: is a bystander effect involved? *Exp Hematol.*, 35(4 suppl. 1):69–77, 2007. (Cited on page 5.)

[17] D. N. Slatkin, P. O. Spanne, F. A. Dilmanian, J. O. Gebbers, and J. A. Laissue. Subacute neuropathological effects of microplanar beams of x-rays from a synchrotron wiggler. *Proc. Natl. Acad. Sci. U.S.A.*, 92:8783–8787, 1995. (Cited on pages 5 and 6.)

[18] P. Regnard, G. Le Duc, E. Bräuer-Krisch, I. Troprès, E. A. Siegbahn, A. Kusak, C. Clair, H. Bernard, D. Dallery, J. A. Laissue, and A. Bravin. Irradiation of intracerebral 9l gliosarcoma by a single array of microplanar x-ray beams from a synchrotron: balance between curing and sparing. *Phys. Med. Biol.*, 53:861–878, 2008. (Cited on pages 5 and 6.)

[19] J. A. Laissue, H. Blattmann, M. Di Michiel, D. N. Slatkin, N. Lyubimova, R. Guzman, W. Zimmermann, S. Birrer, T. Bley, P. Kircher, R. Stettler, R. Fatzer, A. Jaggy, H. Smilowitz, E. Bräuer-Krisch, A. Bravin, G. Le Duc, C. Nemoz, M. Renier, W. C. Thomlinson, J. Stepanek, and H. P. Wagner.

Weanling piglet cerebellum: a surrogate for tolerance to mrt (microbeam radiation therapy) in pediatric neuro-oncology. *Proc. SPIE*, 4508:65–73, 2001. (Cited on pages 5 and 6.)

[20] R. Serduc, Y. Van de Looij, G. Francony, O. Verdonck, B. Van der Sanden, J. A. Laissue, R. Farion, E. Bräuer-Krisch, E. A. Siegbahn, A. Bravin, Y. Prezado, C. Segebarth, C. Rémy, and H. Lahrech. Characterization and quantification of cerebral edema induced by synchrotron x-ray microbeam radiation therapy. *Phys. Med. Biol.*, 53:1153–1166, 2008. (Cited on pages 5 and 6.)

[21] J. A. Laissue, G. Geiser, P. O. Spanne, F. A. Dilmanian, J. O. Gebbers, M. Geiser, X. Y. Wul, M.S. Makar, P. L. Micca, M. M. Nawrocky, D.D. Joel, and D. N. Slatkin. Neuropathology of ablation of rat gliosarcomas and contiguous brain tissues using a microplanar beam of synchrotro-wiggler-generated x-rays. *Int. J. Cancer*, 78, 1998. (Cited on pages 5 and 6.)

[22] F. A. Dilmanian, G. M. Morris, N. Zhong, T. Bacarian, J.F. Hainfeld, J. Kalef-Ezra, L.J. Brewington, J. Tammam, and E. M. Rosen. Murine emt-6 carcinoma: high therapeutic efficacy of microbeam radiation therapy. *Radiat. Res.*, 159(5), 2003. (Cited on page 6.)

[23] M. Garcia-Barros, F. Paris, C. Cordon-Cardo, D. Lyden, S. Rafii, A. Haimovitz-Friedman, Z. Fukus, and R. Kolesnick. Tumor response to radiotherapy regulated by endothelial cell apoptosis. *Science*, 300(5622), 2003. (Cited on page 6.)

[24] P. Baluk, H. Hashizume, and D.M. McDonald. Cellular abnormalities of blood vessels as target in cancer. *Curr. Opin. Genet. Dev.*, 15(1), 2005. (Cited on page 6.)

[25] SPIE Conference proceeding proceeding proceeding proceeding, editor. *Microbeam radiation therapy*, 1999. (Cited on page 6.)

[26] N. Zhong, G. M. Morris, T. Bacarian, E. M. Rosen, and F. A. Dilmanian. Response of rat skin to high-dose unidirectional x-ray microbeams: a histological study. *Radiat. Res.*, 160(2), 2003. (Cited on page 6.)

[27] F. A. Dilmanian, Z. Zhong, T. Bacarian, H. Benveniste, P. Romanelli, R. Wang, J. Welwart, T. Yuasa, E. M. Rosen, and D. J. Anschel. Interlaced x-ray microplanar beams: A radiosurgery approach with clinical potential. *Proc. Natl. Acad. Sci. U.S.A.*, 103(25):9709–9714, 2006. (Cited on page 6.)

[28] Y. Prezado, M. Renier, and A. Bravin. A new method of creating minibeam patterns for synchrotron radiation therapy: a feasibility study. *Journal of Synchrotron Radiation*, 16:582–586, 2009. (Cited on page 6.)

[29] Y. Prezado, S. Thengumpallil, M. Renier, and A. Bravin. X-ray energy optimization in minibeam radiation therapy. *Medical Physics*, 36, 2009. (Cited on pages 6 and 73.)

[30] F. A. Dilmanian, A.L. Jenkins III, J. Olschowka, Z. Zhong, J.Y. Park, N.R. Desnoyers, S. Sobotka, G.R. Fois, C.R. Messina, M. Morales, S.D. Hurley, L. Trojanczyk, S. Ahmad, N. Shahrab, P.K. Coyle, A.G. Meek, and M.K. O'Banion. X-ray microbeam irradiation of the contusion-injured rat spinel cord temporarily improves hind-limb function. *Radiat. Res.*, 179(1):76–88, 2013. in press. (Cited on page 6.)

[31] Y. Prezado, S. Sarun, S. Gil, P. Deman, A. Bouchet, and G. Le Duc. Increase of lifespan for glioma bearing rats by using minibeam radiation therapy. *Journal of Synchrotron Radiation*, 19:60–65, 2012. (Cited on page 7.)

[32] P. Deman, M. Vautrin, M. Edouard, V. Stupar, L. Bobyk, R. Farion, H. Ellaume, C. Remy, E.L. Barbier, Esteve F., and J.F. Adam. Monochromatic minibeams radiotherapy: from healthy tissue-sparing effect studies toward first experimental glioma bearing rats therapy. *Int. J. Radiation Oncology Biol. Phys.*, 82(4), 2012. (Cited on page 7.)

[33] W. Zeman, H.J. Curtis, E.L. Gebhard, and W. Haymaker. Tolerance of mouse brain tissue to high-energy deuterons. *Science*, 130, 1959. (Cited on page 8.)

[34] W. Zeman, H.J. Curtis, and C.P. Baker. Histopathologic effect of high-energy particle microbeams on the visual cortex of the mouse brain. *Radiat. Res.*, 15, 1961. (Cited on pages 8 and 9.)

[35] H.J. Curtis. The use of a deuteron microbeam for simulating the biological effects of heavy cosmic-ray particles. *Radiat. Res.*, 7, 1967. (Cited on page 8.)

[36] R.J. Yaes and A. Kalend. Local stem cell depletion model for radiation myelitis. *Int. J. Radiation Oncology Biol. Phys.*, 14, 1988. (Cited on page 8.)

[37] M. Durante and J.S. Loeffler. Charged particles in radiation oncology. *Nature reviews Clinical Oncology*, 7, 2010. (Cited on pages 10, 11 and 12.)

[38] PAC07, editor. *Status of the hadrontherapy projects in Europe*, 2007. (Cited on page 12.)

[39] M. Tubiana, J. Dutreix, and A. Wambersie. *Introduction to Radiobiology*. Taylor & Francis, 1990. (Cited on page 15.)

[40] E. J. Hall and A. J. Giaccia. *Radiobiology for the radiologist*. Lippincott William & Wilson, 2006. (Cited on pages 16, 17, 21, 24 and 26.)

[41] J. T. Bushberg, J. A. Seibert, E. M. Leidholdt, and J. M. Boone. *The essential physics of medical imaging*. Lippincott William & Wilkins, 2 edition, 2002. (Cited on pages 18 and 19.)

[42] IAEA. *Radiation biology: a handbook for teachers and students*. Vienna, 2010. (Cited on pages 19 and 20.)

[43] M. Belli, O. Sapora, and M. A. Tabocchini. Molecular targets in cellular response to ionizing radiationand implications in space radiation protection. *J. Radiat. Res.*, 43(S13-S19), 2002. (Cited on page 27.)

[44] R. Orecchia, A. Zurlo, A. Loasses, M. Krengli, G.Tosi, S. Zurrida, P. Zucali, and U. Veronesi. Particle beam therapy (hadrontherapy): Basis for interest and clinical experience. *European Journal of Cancer*, 34(4):459–468, 1998. (Not cited.)

[45] P. Marmier and E. Sheldon. *Physics of nuclei and particles*, volume 1. Academic press, New York, 1969. (Cited on pages 36 and 37.)

[46] SNA + MC2010, editor. *New native QMD code in Geant4*, Tokyo, Japan, October 17-21 2010. (Cited on page 39.)

[47] W.V. Tenzel. Experience with grid therapy. *Radiology*, 59, 1952. (Cited on page 75.)

[48] J. Spiga. *Monte Carlo simulation of dose distributins for synchrotron Microbeam Radiation Therapy*. PhD thesis, University of Cagliari, 2007. (Not cited.)

[49] I. Martinez-Rovira. *Monte Carlo and experimental small-field dosimetry applied to spatially fractionated synchrotron radiotherapy techniques*. PhD thesis, Universitat Politecnica da Catalunya, 2012. (Not cited.)

[50] F. Romano. *Monte Carlo simulations of carbon ions fragmentation in hadrontherapy*. PhD thesis, University of Catania, 2008. (Not cited.)

[51] F. James. Monte carlo theory and practice. *Rep. Prog. Phys.*, 43:1145–1189, 1980. (Cited on page 32.)